Title
Top-down isoprene emissions over tropical South America inferred from SCIAMACHY and OMI formaldehyde columns

Journal
Journal of Geophysical Research: Atmospheres, 118(12)

ISSN
2169-897X

Authors
Barkley, Michael P
De Smedt, Isabelle
Van Roozendael, Michel
et al.

Publication Date
2013-06-27

DOI
10.1002/jgrd.50552

JOURNAL OF GEOPHYSICAL RESEARCH: ATMOSPHERES, VOL. 118, 6849–6868, doi:10.1002/jgrd.50552, 2013

Top-down isoprene emissions over tropical South America inferred from SCIAMACHY and OMI formaldehyde columns

Michael P. Barkley,[1] Isabelle De Smedt,[2] Michel Van Roozendael,[2] Thomas P. Kurosu,[3,4] Kelly Chance,[3] Almut Arneth,[5,6] Daniel Hagberg,[5] Alex Guenther,[7] Fabien Paulot,[8] Eloise Marais,[8] and Jingqiu Mao[9]

Received 22 October 2012; revised 4 April 2013; accepted 2 June 2013; published 27 June 2013.

[1] We use formaldehyde (HCHO) vertical column measurements from the Scanning Imaging Absorption spectrometer for Atmospheric Chartography (SCIAMACHY) and Ozone Monitoring Instrument (OMI), and a nested-grid version of the GEOS-Chem chemistry transport model, to infer an ensemble of top-down isoprene emission estimates from tropical South America during 2006, using different model configurations and assumptions in the HCHO air-mass factor (AMF) calculation. Scenes affected by biomass burning are removed on a daily basis using fire count observations, and we use the local model sensitivity to identify locations where the impact of spatial smearing is small, though this comprises spatial coverage over the region. We find that the use of the HCHO column data more tightly constrains the ensemble isoprene emission range from 27–61 Tg C to 31–38 Tg C for SCIAMACHY, and 45–104 Tg C to 28–38 Tg C for OMI. Median uncertainties of the top-down emissions are about 60–260% for SCIAMACHY, and 10–90% for OMI. We find that the inferred emissions are most sensitive to uncertainties in cloud fraction and cloud top pressure (differences of ±10%), the a priori isoprene emissions (±20%), and the HCHO vertical column retrieval (±30%). Construction of continuous top-down emission maps generally improves GEOS-Chem's simulation of HCHO columns over the region, with respect to both the SCIAMACHY and OMI data. However, if local time top-down emissions are scaled to monthly mean values, the annual emission inferred from SCIAMACHY are nearly twice those from OMI. This difference cannot be explained by the different sampling of the sensors or uncertainties in the AMF calculation.

Citation: Barkley, M. P., et al. (2013), Top-down isoprene emissions over tropical South America inferred from SCIAMACHY and OMI formaldehyde columns, *J. Geophys. Res. Atmos.*, *118*, 6849–6868, doi:10.1002/jgrd.50552.

1. Introduction

[2] It is well established that terrestrial vegetation emit a diverse range of reactive biogenic volatile organic compounds (BVOCs) into the atmosphere, which serve important roles in the biosphere and which influence atmospheric chemistry and climate [*Kesselmeier and Staudt*, 1999; *Laothawornkitkul et al.*, 2009]. The most important of these compounds is isoprene, whose global emissions of 400–600 Tg C a^{-1} comprise approximately half of the total BVOC budget [*Guenther et al.*, 1995, 2006; *Arneth et al.*, 2008]. Isoprene has a significant impact on tropospheric photochemistry, by influencing the formation of tropospheric ozone [*Paulot et al.*, 2012] and secondary organic aerosol [*Kanakidou et al.*, 2005] and by affecting the oxidation capacity of the atmosphere [*Lelieveld et al.*, 2008; *Taraborrelli et al.*, 2012]. Isoprene emissions are highly uncertain [*Arneth et al.*, 2008], especially from tropical regions where there is a notable lack of observational data to constrain current bottom-up models [e.g., *Guenther et al.*, 2006; *Arneth et al.*, 2007; *Lathière et al.*, 2010]. Given that tropical ecosystems may contribute up to 75% of global

Additional supporting information may be found in the online version of this article.

[1]EOS Group, Department of Physics and Astronomy, University of Leicester, Leicester, UK.
[2]Belgian Institute for Space Aeronomy (BIRA-IASB), Brussels, Belgium.
[3]Harvard-Smithsonian Center for Astrophysics, Cambridge, Massachusetts, USA.
[4]Now at Jet Propulsion Laboratory, Pasadena California, USA.
[5]Department of Physical Geography and Ecosystems Analysis, Geobiosphere Science Center, Lund University, Lund, Sweden.
[6]Atmospheric Environmental Research/Institute of Meteorology and Climate Research, Karlsruhe Institute of Technology, Karlsruhe, Germany.
[7]National Center of Atmospheric Research, Boulder, Colorado, USA.
[8]Earth and Planetary Sciences, Harvard University, Cambridge, Massachusetts, USA.
[9]Geophysical Fluid Dynamics Laboratory, Princeton University, Princeton, New Jersey, USA.

Corresponding author: M. P. Barkley, EOS Group, Department of Physics and Astronomy, University of Leicester, Leicester, LE1 7RH, UK. (mpb14@le.ac.uk)

2169-897X/13/10.1002/jgrd.50552

annual emissions [*Guenther et al.*, 2006], it is paramount that we accurately quantify their emissions and acquire a better understanding of the factors which affect emission variability [*Arneth et al.*, 2011]. The Amazon Basin, which covers over five million square kilometers and contains the world's largest rainforest, may account for up to 35% of the total global emissions alone [*Barkley et al.*, 2011], making it the Earth's largest single source region. In spite of this, there have been only a small number of short-duration Amazon field campaigns that have made (or inferred) measurements of localized isoprene fluxes [see, e.g., *Kuhn et al.*, 2004, 2007; *Karl et al.*, 2007]. Knowledge of isoprene emissions from the entire Amazon Basin over a complete seasonal cycle is therefore limited.

[3] Top-down isoprene emission estimates derived from satellite observations of formaldehyde (HCHO) vertical columns [e.g., *Barkley et al.*, 2008; *Stavrakou et al.*, 2009a], can potentially bridge this data gap, since HCHO is a high-yield product of isoprene oxidation and contains the signature of localized isoprene emissions on spatial scales of order ∼10–100 km [*Palmer et al.*, 2003; *Turner et al.*, 2012]. However, inference of top-down emissions over tropical regions is a challenge owing to the following: (1) uncertainties in the HCHO vertical column retrieval, (2) removal of biomass burning contributions from the HCHO columns, and (3) large uncertainties in the complex isoprene oxidation chemistry that occurs in the low nitrogen oxide (NO_x) conditions [*Archibald et al.*, 2010].

[4] In addition to the HCHO spectral fitting itself, uncertainties in the HCHO column retrieval also arise through the computation of the air-mass factor (AMF), which converts retrieved slant columns (viewed along the instrument's line-of-sight) to vertical columns [*Palmer et al.*, 2001]. The AMF requires knowledge of each scene's cloud coverage, surface reflectance, and the vertical distribution of aerosols and HCHO, the latter two parameters usually being taken from a chemistry-transport model (CTM), driven by a specified bottom-up isoprene emission inventory. In our previous work, we examined the HCHO vertical column sensitivity to various AMF input parameters [*Barkley et al.*, 2012], using HCHO column measurements over the Amazon retrieved by the Scanning Imaging Absorption spectrometer for Atmospheric Chartography (SCIAMACHY) [*Bovensmann et al.*, 1999], and the Ozone Monitoring Instrument (OMI) [*Levelt et al.*, 2006]. Although clouds were identified as the dominant AMF error, the use of different a priori isoprene emissions, through their impact on the HCHO profile used in the AMF calculations, could produce sizeable differences in the resulting HCHO vertical columns (typically ±20%). Similar uncertainties were also found due to variations in surface reflectance and aerosol loading, though biomass burning aerosols distributed high above the boundary layer resulted in much greater changes in the HCHO columns (up to +50%).

[5] Although the oxidation of isoprene is the main driver of HCHO column variability over the Amazon rainforest [*Barkley et al.*, 2008; *Stavrakou et al.*, 2009b], HCHO directly emitted from biomass burning, along with oxidation of other co-released VOCs, can result in large localized enhancements. Determination of top-down isoprene emissions therefore requires either isolation of biogenic contributions to the HCHO columns [*Barkley et al.*, 2008; *Marais et al.*, 2012], or simultaneous inversion of both biogenic and pyrogenic emissions [*Stavrakou et al.*, 2009a]. Removal of the biomass burning signal has previously been partly achieved using observation of colocated Along Track Scanning Radiometer (ATSR) fire counts and elevated nitrogen dioxide (NO_2) columns [e.g., *Barkley et al.*, 2008, 2009], both of which are active tracers of burning vegetation, despite issues with ATSR temporal sampling (night time measurements only) and determining a robust NO_2 threshold. Discarding fire-affected scenes can be advantageous as it compensates for AMF uncertainties due to biomass burning aerosols, but this is typically offset by a loss in spatial coverage.

[6] To interpret the satellite HCHO data requires a CTM that can adequately simulate Amazonian tropospheric photochemistry and other physical processes. However, the oxidation of isoprene in low-NO_x conditions (<1 ppbv) is particularly uncertain. Consequently, there have been a large number of recent studies examining its atmospheric degradation [e.g., *Paulot et al.*, 2009a, 2009b; *Taraborrelli et al.*, 2009; *Lockwood et al.*, 2010; *Crounse et al.*, 2011; *Paulot et al.*, 2012] and its role in the recycling of hydroxyl (OH) and hydroperoxyl (HO_2) radicals [e.g., *Lelieveld et al.*, 2008; *Peeters et al.*, 2009; *Peeters and Müller*, 2010; *Mao et al.*, 2012; *Taraborrelli et al.*, 2012]. For deriving top-down emissions, the crucial aspect is the short-term HCHO yield from isoprene oxidation [*Palmer et al.*, 2003]. In low-NO_x environments, isoprene peroxy radicals ($ISOPO_2$) formed from the initial reaction of isoprene with OH, can react with HO_2 slowing local photochemistry via the formation of organic hydroperoxides. This effect can result in spatial smearing that makes it potentially difficult to directly relate emitted isoprene with observed HCHO columns using a local linear relationship [*Marais et al.*, 2012; *Paulot et al.*, 2012; *Turner et al.*, 2012]. That said, the observed variability of previous top-down estimates during the Amazon dry season, derived using a local-relationship, were consistent with the known temperature dependence of isoprene emissions, suggesting some degree of confidence in this approach [*Barkley et al.*, 2008].

[7] In this work we present a new set of top-down isoprene emissions for tropical South America, derived from SCIAMACHY and OMI HCHO columns in 2006, a crossover time period when each instrument's performance is stable and when biomass burning in the Amazon is less prevalent. To infer the top-down isoprene emissions from the observed HCHO columns, we use a recently developed nested-grid version of the GEOS-Chem CTM [*Barkley et al.*, 2011], which we run with different bottom-up isoprene emission inventories chemical mechanisms, and boundary layer mixing schemes, to produce an ensemble of top-down estimates using the methodology of *Palmer et al.* [2003]. While we recognize some of the potential shortcomings of this approach (e.g., each grid cell is treated independently), it allows fast derivation of top-down emissions from numerous model simulations, enabling us to produce a range of estimates to characterize associated uncertainties. In addition, we pay careful attention to the removal of biomass burning scenes using gridded fire count data from AATSR, and also from the MODIS instruments onboard NASA's EOS-Aqua and EOS-Terra satellites, filtering the HCHO columns observations at different temporal resolutions (daily, eight day

and monthly) and quantifying the effect on the top-down emissions. A full Bayesian inversion [e.g., *Stavrakou et al.*, 2009a] will be the focus of our future work, permitting a direct comparison with the estimates produced by this more simplistic method.

[8] In sections 2 and 3, we provide an overview of the GEOS-Chem model, and describe the SCIAMACHY and OMI HCHO slant column retrievals and their AMF calculations. In section 4, we outline the method used to determine the top-down emissions, including our approach for removing HCHO columns influenced by biomass burning. In section 5, we present our new top-down estimates and discuss their associated errors, including a sensitivity analysis in section 6. Finally, we examine the impact of the top-down isoprene emissions on GEOS-Chem's simulation of HCHO over the Amazon in section 7, as well as comparing the SCIAMACHY and OMI estimates in section 8, before concluding the paper in section 9.

2. GEOS-Chem

2.1. Overview

[9] We use the GEOS-Chem chemistry-transport model (v8-03-01) in a one-way nested grid mode, as our intermediary to infer top-down emissions from the observed HCHO vertical columns over tropical South America (approximately 30°–85°W, 14°N–25°S). As a full description of the model is provided in *Barkley et al.* [2011], we only provide key details here. The nested-grid has a horizontal resolution of 0.667° × 0.5° (longitude × latitude) and has 47 hybrid eta levels extending from the surface to 0.01 hPa. The boundary layer up to 2 km resolved by 14 layers, with tracers fully mixed (unless otherwise stated) at each chemistry time step (60 min). The model is driven using Goddard Earth Observing System (GEOS-5) assimilated meteorology [*Rienecker et al.*, 2008], which is updated every 6 h for three-dimensional variables and every 3 h for surface fields and mixing depths. Boundary conditions to the nested-grid are provided every 3 h from an off-line global 4° × 5° simulation. Biomass burning emissions are based on the Global Fire Emission Database (GFED v2) [*van der Werf et al.*, 2006]; other surface emissions for the domain are described in *Barkley et al.* [2011].

2.2. BVOC Emission Inventories

[10] The nested-grid can be driven using two different isoprene emission inventories: (1) the canopy-scale Model of Emissions of Gases and Aerosols from Nature (MEGAN) or (2) the leaf-scale algorithm of *Arneth et al.* [2007] coupled to the Lund-Potsdam-Jena General Ecosystem Simulator (LPJ-GUESS) dynamic vegetation model (DVM). MEGAN emissions are calculated using empirical algorithms, which account for current and past conditions in the canopy environment, applied to gridded basal emission capacities [*Guenther et al.*, 2006]; seasonal variations in leaf area are based on MODIS leaf area index (LAI) [see *Barkley et al.*, 2011]. The LPJ-GUESS model differs in that leaf-level emission capacities assigned for different plant functional types, and the DVM itself is used to simulate seasonal variations in vegetation and to upscale leaf emissions to the ecosystem level. Daily emissions are calculated, adopted from *Niinemets et al.* [1999] and are translated into sub-daily patterns following a light and temperature response that is analogous to the response used by *Guenther et al.* [1995]. In this work we drive GEOS-Chem with five different isoprene emission scenarios using different variants of the MEGAN and LPJ-GUESS inventories, summarized in Table 1 and described in detail in *Barkley et al.* [2011]. The isoprene emissions predicted by each model are dependent on (a) their assignment of basal emission capacities, (b) the algorithms that drive temporal variability, and (c) the specified vegetation distribution and its leaf-area. All three parameters are not well constrained for tropical ecosystems, and large differences in the magnitude and distribution of Amazon isoprene emissions were found from the MEGAN and LPJ-GUESS inventories [*Barkley et al.*, 2011]. In particular, emissions from MEGAN were generally higher than from LPJ-GUESS, and whereas MEGAN had emission hot spots deep within the rainforest along the western Brazilian border, LPJ-GUESS emissions were highest in south eastern regions of the continent [see, e.g., *Barkley et al.*, 2011, Figure 2].

2.3. Chemical Scheme

[11] Based on a previous model evaluation against in situ observations in the Amazon [*Barkley et al.*, 2011], we use an updated GEOS-Chem chemical mechanism following the work of *Paulot et al.* [2009a, 2009b]. This scheme contains about 400 reactions and 80 species (56 of which are transported), integrated using the SMVGEAR solver of *Jacobson* [1995]. Photolysis rates are calculated using the Fast-J algorithm of *Wild et al.* [2000]; wet deposition of aerosols and gases are described in *Liu et al.* [2001] and *Mari et al.* [2000], respectively. Dry deposition is based on the standard resistance-in-series model of *Wesely* [1989], as described in *Wang et al.* [1998] and updated in *Barkley et al.* [2011]. The chemical scheme provides a relatively detailed treatment of isoprene oxidation, including the reactions, transport and deposition of isoprene epoxides and hydroperoxides, as well as isoprene, methacrolein (MACR) and methyl vinyl ketone (MVK) nitrates. Nevertheless, modeled isoprene oxidation products are typically overestimated and HO_x(= OH + HO_2) underestimated when compared with observations from the TROFFEE [*Karl et al.*, 2007] and GABRIEL [*Stickler et al.*, 2007] field campaigns [see *Barkley et al.*, 2011]. *Peeters et al.* [2009] and *Peeters and Müller* [2010] have proposed that isoprene peroxy isomerization reactions may outcompete traditional NO or HO_2 pathways, regenerating HO_x and producing hydroperoxy aldehydes (HPALDs) that further generate HO_x through fast photolysis. We therefore include two tests in our analysis to examine the sensitivity of inferred top-down isoprene emissions to this new reaction mechanism. First, we follow the work of *Paulot et al.* [2012] by assuming *direct* photolysis of HPALDs, using the rate suggested by *Crounse et al.* [2011]. Second, we modify our scheme to *explicitly* include HPALDs, using the reaction rate coefficients and yields suggested by *Stavrakou et al.* [2010] and *Peeters and Müller* [2010], for the two main isoprene radical channels (β-hydroxyperoxys $ISOPBO_2$ and $ISOPDO_2$), accepting that these rates and products are still very uncertain. For this analysis we additionally update several key chemical rates including (a) reactions of HO_2 with $>C_2$ peroxy radicals [*Saunders et al.*, 2003, equation (vi)], (b) initial reactions of

Table 1. The Ensemble of GEOS-Chem Scenarios

Scenario	Description
PCEEA	Default scenario for each instrument. Isoprene emissions calculated using the PCEEA algorithm of *Guenther et al.* [2006]
HYBRID	Isoprene emissions calculated using a five-layer canopy model and a combination of *Guenther et al.*, [1999, 2006] algorithms[a]
MULLER	As HYBRID, but with isoprene emissions scaled by 0.635 to be consistent with the study of *Müller et al.* [2008][b]
LPJ-G5	Emissions based on the LPJ-GUESS model forced with GEOS-Chem's GEOS-5 meteorology
LPJ-CRU	Emissions based on the LPJ-GUESS model forced with its default CRU meteorology[c]
BL	As the default scenario but with a non-local boundary layer mixing scheme employed in GEOS-Chem[d]
SLOWDEP	As the default scenario but without the fast deposition of oxygenated VOCs[e]
HPALD	As the default scenario but assuming fast photolysis of hydroperoxy aldehydes[f]
LIM0	As the default scenario but with the explicit treatment of hydroperoxy aldehydes[g]
CHEMT	As the default scenario but using a 10 min emission and chemistry time step (instead of 60 min)
ALB	As the default scenario but using the *Herman and Celarier* [1997] surface reflectances in the AMF computation
CF+	As the default scenario, but assuming a +0.1 cloud fraction error in the AMF computation[h]
CF–	As the default scenario, but assuming a –0.1 cloud fraction error in the AMF computation[h]
CTP+	As the default scenario, but assuming a +60 hPa error in cloud top pressure in the AMF computation[h]
CTP–	As the default scenario, but assuming a –60 hPa error in cloud top pressure in the AMF computation[h]

[a]This (hybrid) emission scheme, which uses MEGAN v2.1 basal emission factors, is fully described in *Barkley et al.* [2011].
[b]The 0.635 scaling factor is the average difference between the HYBRID and *Müller et al.* [2008] monthly mean emissions over both 2005 and 2006 [see *Barkley et al.*, 2011].
[c]Data from the Climate Research Unit of the University of East Anglia (http://www.cru.uea.ac.uk/).
[d]The non-local scheme includes "local" mixing between adjacent model layers and, depending on the stability of the PBL, "non-local" mixing due to turbulent eddies [*Lin and McElroy*, 2010].
[e]Normal dry deposition are assumed by setting the reactivity factors of OVOCs to 0.1.
[f]HO_x regeneration from the fast photolysis of HPALDs follows *Paulot et al.* [2012];
[g]The treatment of HPALDs is explicitly included in the chemical scheme following *Stavrakou et al.* [2010].
[h]Estimated uncertainties based on the study of *Acarreta et al.* [2004], and are applied to each HCHO observation [*Barkley et al.*, 2012].

isoprene with OH, O_3, and the nitrate radical (NO_3) [*Sander et al.*, 2011], and (c) the formation of nitric acid (HNO_3) from OH and NO_2 [*Mollner et al.*, 2010]. We also incorporate the fast deposition of oxygenated VOCs (including MVK, MACR, and HCHO) based on the work of *Karl et al.* [2010]. We find that the subsequent HCHO yields from isoprene oxidation resulting from these new updates are within 5% of those presented in *Barkley et al.* [2011] and discuss them in more detail in section 4.3.

3. SCIAMACHY and OMI HCHO Columns

3.1. Retrieval of HCHO Slant Columns

[12] In this study we use HCHO slant columns retrieved by SCIAMACHY and OMI. Here we only summarize the key aspects (Table 2), and refer the reader to the appropriate references for full details.

[13] SCIAMACHY is a UV-VIS-NIR grating spectrometer on board ESA's ENVISAT satellite, which is in a polar sun-synchronous orbit crossing the Equator at 10:00 local time (LT). SCIAMACHY has a ground swath of 960 × 30 km^2 (across × along track) and makes alternating nadir and limb measurements. The nominal nadir pixel size is 60 × 30 km^2 resulting in global coverage within about 6 days. HCHO slant columns are retrieved from a fitting window of 328.5–346 nm using differential optical absorption spectroscopy, as described in *De Smedt* [2011]. The absorption cross sections of HCHO and other interfering gases are fitted, along with corrections for the Ring effect, a linear intensity offset, and a fifth-order polynomial closure term.

[14] OMI is a nadir-viewing near-UV/visible charged-couple device spectrometer on board NASA's EOS-Aura satellite, also in a sun-synchronous polar orbit, but with an Equator crossing time of 13:30 LT. OMI has a 2600 km wide swath which contains 60 cross-track pixels that range in size from 13×24 km^2 at nadir, to 28×160 km^2 at the swath edges. OMI HCHO slant columns are retrieved from the direct fitting of radiances in the interval 327.5–356.5 nm, using a non-linear least-squares algorithm, as described in *Chance* [2002] and *Kurosu and Chance* [2008]. The OMI retrieval also includes on-line solar and radiance wavelength calibration, an under-sampling correction, computation of common model residual spectrum, and a destriping algorithm to reduce cross-track noise.

[15] Over tropical South America, the uncertainties of a single HCHO slant column observation typically range from about 20–300% for SCIAMACHY, and 10–200% for OMI, for slant columns exceeding the global background ($\sim 4 \times 10^{15}$ molecules cm^{-2}).

3.2. Reference Sector Correction

[16] Since both retrievals use a daily radiance reference spectrum in lieu of a solar irradiance spectrum, the retrieved HCHO slant columns (Ω_s) only represent the difference with respect to the slant column contained in the radiance reference [*De Smedt et al.*, 2008; *Kurosu and Chance*, 2008]. We, therefore, apply an absolute normalization to the HCHO slant columns on a daily basis. First, the median slant column (Ω_{s_0}) over the remote Pacific Ocean (110°–140°W, 15°N–15°S) is subtracted from all retrieved slant columns. Second, a model daily HCHO background (Ω_{v_B}) over the same Pacific region, taken from a global GEOS-Chem simulation, is then added back to the retrieved HCHO vertical columns after the application of the air mass factor (M) to renormalize the vertical columns (Ω_v) as follows:

$$\Omega_v = \frac{(\Omega_s - \Omega_{s_0})}{M} + \Omega_{v_B} = \frac{\Omega_s^R}{M} + \Omega_{v_B} \quad (1)$$

where $\Omega_s^R = \Omega_s - \Omega_{s_0}$. Over the Pacific Ocean, the HCHO background is assumed to be well characterized; hence, this approach ensures that both retrievals are consistently

Table 2. Summary of the SCIAMACHY and OMI Instruments and Their HCHO Retrievals

	SCIAMACHY	OMI
	Instrument	
Platform	ENVISAT	EOS-Aura
Orbit	Sun-synchronous, descending node	Sun-synchronous, ascending node
Local Equator crossing time	10:00	13:30
Swath	960 km	2600 km
Main observing mode	Alternating limb/nadir sequence	Continuous nadir
Pixel size (at nadir)	30×60 km^2	13×24 km^2
Global coverage	6 days	1 day
Spectral range	220–2380 nm	270–500 nm
	HCHO retrieval	
Fitting window	328.5–346 nm	327.5–356.5 nm
Spectral resolution (at 340 nm)	0.26 nm	0.42 nm
Fitting method	DOAS	Direct radiance fitting
Solar I_0[a]	Daily radiance reference	Daily radiance reference
Fitted species[b]	HCHO, O_3, O_4, NO_2, BrO, Ring, OClO	HCHO, O_3, NO_2, BrO, Ring
HCHO cross-section	*Meller and Moortgat* [2000] at 298 K	*Cantrell et al.* [1990] at 300 K
Closure polynomial	Fifth order	Third order
Undersampling correction	No	Yes
Additional fit parameters	Linear offset correction	Common-mode residual
References	*De Smedt et al.* [2008]; *De Smedt* [2011]	*Chance* [2002]; *Kurosu and Chance* [2008]
Cloud algorithm	FRESCO v5 [*Wang et al.*, 2008]	OMI O_2-O_2 [*Acarreta et al.*, 2004]

[a]Taken from over the equatorial Pacific Ocean.
[b]Both retrievals fit the Ring spectrum following the method of *Chance and Spurr* [1997].

normalized. It also removes an increasing background trend in the OMI retrieval, possibly associated with a drift in the instrument's dark current [*Fortems-Cheiney et al.*, 2012]. Similar reference sector corrections have been used in other studies [e.g., *Palmer et al.*, 2006; *Barkley et al.*, 2008; *De Smedt et al.*, 2008; *Gonzi et al.*, 2011; *Marais et al.*, 2012].

3.3. Calculation of HCHO Vertical Columns

[17] We compute AMF look-up tables for SCIAMACHY and OMI using monthly averaged HCHO profiles and aerosol optical depths (AOD) from each GEOS-Chem simulation, appropriate to each instrument's overpass time. The AMFs are computed at a wavelength of 340 nm (consistent with the model AOD) using corresponding aerosol optical properties based on the initial work of *Martin et al.* [2003]. These model profiles are provided to the radiative transfer model LIDORT [*Spurr et al.*, 2001], which calculates scattering weights that describe the sensitivity of the measurement to the amount of HCHO at each altitude, while also being independent of the profile shape [*Palmer et al.*, 2001]. Each look-up table is parameterized as a function of location (surface pressure), solar zenith angle, cloud-top pressure, and viewing geometry. Partially cloudy scenes are accounted for using the independent pixel approach of *Martin et al.* [2002]. Clouds are treated as Lambertian reflectors with an albedo of 0.8 [*Chance*, 2002]. The surface reflectance at 342 nm for clear sky conditions is taken from the OMI climatology derived by *Kleipool et al.* [2008]. The cloud fraction (CF) and cloud-top pressure (CTP) for each observation are provided by the respective SCIAMACHY FRESCO v5 [*Wang et al.*, 2008], and OMI O_2-O_2 [*Acarreta et al.*, 2004] cloud algorithms. Scenes with > 40% cloud cover are excluded from our analysis. Once calculated, the AMFs are applied to the HCHO slant columns using equation (1).

[18] We additionally filter the OMI HCHO data excluding observations that do not satisfy standard quality checks [*Kurosu and Chance*, 2008] and which are affected by the documented OMI row anomaly (see http://www.knmi.nl/omi/research/product/rowanomaly-background.php). We also find that SCIAMACHY is quite badly affected by the South Atlantic Anomaly (SAA) [*Nichitiu et al.*, 2004], resulting in particularly noisy HCHO measurements over southeastern areas of our domain. Subsequently, we remove observations in compromised grid cells using the approach of *Stavrakou et al.* [2009a]; no correction is made for OMI as it is not affected.

3.4. HCHO Vertical Column Uncertainties

[19] *De Smedt et al.* [2008] showed that the total error on each HCHO vertical column (ϵ_v) can be expressed as follows:

$$\epsilon_v^2 = \frac{1}{M^2}\epsilon_s^2 + \left(\frac{\Omega_s^R}{M^2}\right)^2 \epsilon_M^2 + \epsilon_{v_B}^2 \quad (2)$$

where sources of error in the HCHO vertical columns include uncertainties in (1) the slant column fitting (ϵ_s), (2) the AMF calculation (ϵ_M), and (3) the reference sector correction (ϵ_{v_B}). Spectral fitting errors arise because of uncertainties in the trace gas absorption cross sections, instrumental issues or because of systematic misfit effects (e.g., strong ozone interference). Sources of uncertainty in the AMF include uncertainties in the aerosol loading, cloud fraction, cloud-top pressure, surface reflectance, and the HCHO vertical distribution, which is influenced by the a priori isoprene emissions and other model uncertainties (e.g., chemical mechanism, boundary-layer mixing). Based on our previous AMF analysis [*Barkley et al.*, 2012], for each of these error terms, we assign the following uncertainties over our region of interest: HCHO profile (20%), aerosols (20%), cloud fraction (30%), cloud-top pressure (20%), surface reflectance (20%), and boundary-layer mixing (10%). Added in quadrature, we estimate the total uncertainty in the AMF to be realistically about 50%. Finally, we estimate the error ϵ_{v_B} to be a maximum of

50% ($\sim 2 \times 10^{15}$ molecules cm^{-2}) based on the work of *De Smedt et al.* [2008]. By applying these upper limit uncertainties and taking into account that on average there are six SCIAMACHY and 134 OMI observations per grid cell per month, we find monthly averaging onto the GEOS-Chem grid results in median HCHO vertical column errors of 40–60% for SCIAMACHY and 5–15% for OMI, assuming the errors are truly random. In practice, unknown systematic biases in the HCHO data may exist.

4. Inference of Top-Down Emissions

4.1. Methodology

[20] Inference of top-down isoprene emissions from satellite HCHO column observations is based on a linear regression between model isoprene emissions E'_{isop} (atom C cm^{-2} s^{-1}) and HCHO columns (Ω'_v) that have been sampled along the orbital track and averaged on the model grid:

$$\Omega'_v = SE'_{\text{isop}} + B \quad (3)$$

The slope S (units of s) represents the HCHO produced from the emission of isoprene, and the intercept B represents the diffuse HCHO background from the oxidation of methane and other long-lived VOCs [*Palmer et al.*, 2003]. Top-down isoprene emissions, E_{Isop}, can then be derived from the observed HCHO columns by simply transposing equation (3) and substituting in the satellite HCHO columns (Ω_v), i.e., $E_{\text{isop}} = (\Omega_v - B)/S$. This method has been used in several studies focussing on non-tropical environments [see, e.g., *Palmer et al.*, 2003, 2006; *Millet et al.*, 2008; *Fu et al.*, 2007], where strong correlations ($r > 0.9$) between E'_{Isop} and Ω'_v indicates rapid local HCHO production from isoprene oxidation and negligible spatial smearing. However, application of this method over tropical regions first requires removal of scenes influenced by biomass burning and then identification of grid squares where spatial smearing is minimal. Furthermore, any inferred emissions are dependent on the choice of model configuration, since this influences the fitted regressions values and the a priori information provided to the AMF calculation. To characterize this model uncertainty, we therefore determine a set of top-down emissions based on different assumptions in GEOS-Chem and the subsequent AMF computation, as described in Table 1, to quantify the impact on the inferred estimates and to establish which parameters have the greatest effect. The different scenarios test processes likely to affect the isoprene-HCHO relationship including the choice of initial a priori isoprene inventory and boundary layer mixing scheme [*Barkley et al.*, 2011], the formation of HPALDs and subsequent HO_x generation within the isoprene oxidation mechanism [*Stavrakou et al.*, 2010], the sensitivity to oxygenated VOC dry deposition [*Karl et al.*, 2010], and finally the model time step [*Ashworth et al.*, 2010]. The sensitivity of the top-down emissions to uncertainties in the surface reflectance, cloud fraction and cloud-top pressure within the AMF calculation are also examined [*Barkley et al.*, 2012]. For each scenario, the model has a 6 month spin-up (initialized from a previous year-long simulation) and uses boundary constraints from a global simulation based on the same isoprene emission inventory. AMFs are recalculated for each individual simulation and applied to the retrieved slant columns to generate HCHO vertical columns consistent with the model regression.

4.2. Removal of Biomass Burning Signal

[21] To detect biomass burning and wild fires we use observations of active burning from the Advanced ATSR (AATSR) instrument on-board ENVISAT (algorithm 1 of the World Fire Atlas [*Arino et al.*, 2005]), and the Aqua and Terra MODIS instruments [*Giglio et al.*, 2003]. AATSR only detects fires during the night (around 22:00 LT), where as the MODIS instruments detect fires twice daily (Terra 10:30 and 22:30 LT; Aqua 13:30 and 01:30 LT). Our default procedure to remove fire affected scenes is to construct daily fire masks using the raw AATSR and MODIS (products MYD14 and MOD14, collection 5) active fire count observations. Here we adopt a zero tolerance approach by using all observations (irrespective of detection confidence) thereby accepting potential misidentifications due to persistent hot spots or clouds [*Giglio et al.*, 2006]. To account for the transport of HCHO from biomass burning we discard any SCIAMACHY and OMI HCHO column observation if a fire occurs in either the grid cell in which it falls, or in those immediately adjacent (within ± 1 grid cell), of both the concurrent or preceding day. During the dry season this fire-screening can remove up to 45% of land grid cells for SCIAMACHY and up to only 25% for OMI (owing to its more frequent sampling).

4.3. Spatial Smearing

[22] Since isoprene is emitted in large quantities from the rainforest and has a short lifetime, it largely determines HCHO column variability over the Amazon, despite lower ultimate HCHO yields in the low NO_x conditions [*Barkley et al.*, 2008, 2009; *Stavrakou et al.*, 2009a, 2009b]. However, application of equation (3) requires the modeled and observed HCHO columns to be directly related to isoprene emission within the same model grid square. Thus, sufficiently fast HCHO production and minimal horizontal transport are both necessary for equation (3) to be valid. However, our initial tests of this method resulted in only moderate correlations between the model isoprene emissions and HCHO columns over the ensemble (mean correlation $\bar{r} \sim 0.7$ and range 0.34–0.93), which might indicate that this local relationship no longer holds. We therefore examine the HCHO formation rate and the extent of spatial smearing over this domain.

[23] Since in our analysis we average the model data over a symmetrical time window around the overpass of each instrument (SCIAMACHY 9–11 LT and OMI 12–15 LT), we show in Figure 1 the GEOS-Chem cumulative HCHO yields from a separate pulse release of 1 ppbv of isoprene at 09:00 and 12:00 LT under different NO_x loadings. The corresponding yields are presented in Table 3. GEOS-Chem boundary layer NO_x mixing ratios are typically 0.01–0.5 ppbv after screening for fires; hence, HCHO production occurs in general at relatively low NO_x. However, it is evident that even when NO_x is very low, there is still rapid HCHO production within the first couple of hours; typically 25–50% of the ultimate yield. In reality the actual amount of HCHO produced will depend on the local conditions. For example, if NO_x is held constant at 0.05 ppbv, the HCHO yields at 11:00 and 15:00 are 0.11 and 0.17 per

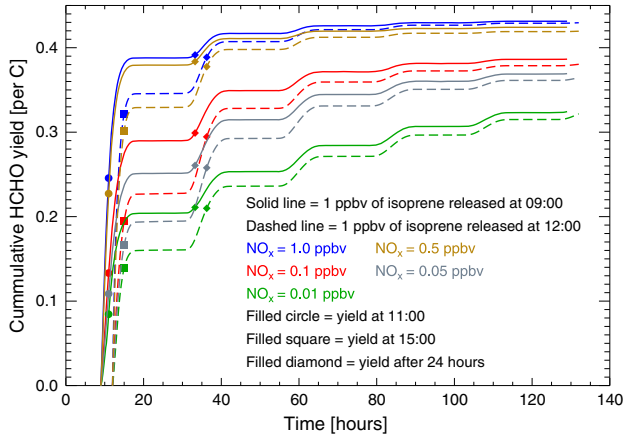

Figure 1. GEOS-Chem cumulative HCHO yields (per C) calculated by a photochemical box model based on the pulse release of 1 ppbv of isoprene at 09:00 and 12:00 (in separate simulations) under different constant NO_x regimes. Yields at specific times are given in Table 3. Full details of the box model simulation can be found in *Barkley et al.* [2011].

C (i.e., 0.55 and 0.85 ppbv of HCHO). Since a typical emission rate of 5×10^{12} atoms C cm^{-2} s^{-1} and a boundary layer height of 1000 m constitutes about 3–4 ppbv of isoprene in the atmosphere, approximately 1–4 ppbv of HCHO could be produced in the lower troposphere by the time SCIAMACHY and OMI are overhead, perturbing the HCHO column by an amount that is generally within the uncertainty of the monthly gridded HCHO observations (potentially up to 10–80%; see, e.g., *Barkley et al.* [2011], Figure 8).

[24] Determination of the smearing length is a more important consideration. Two length scale metrics define critical distances relative to the model spatial dimensions: (1) the displacement distance L_d, which is the distance from the point of emission at which HCHO produced from the VOC oxidation is a maximum; and (2) the smearing distance L_s, which is the distance at which the HCHO column reaches $(1 - 1/e)$ of its ultimate value [*Palmer et al.*, 2003]. The displacement length can be determined from

$$L_d = \frac{U}{(k_{\mathrm{Isop}} - k_{\mathrm{HCHO}})} \ln\left(\frac{k_{\mathrm{Isop}}}{k_{\mathrm{HCHO}}}\right) \quad (4)$$

and when the VOC lifetime is shorter than the HCHO column lifetime, as is the case for isoprene, the amount of smearing can be estimated by U/k_{HCHO} [*Palmer et al.*, 2003]; k_{Isop} and k_{HCHO} are the isoprene and HCHO loss rate constants, and U is the average wind speed. At the time of each satellite overpass, model HCHO column lifetimes are around 2–2.5 h and corresponding median tropospheric wind speeds are 1–20 km h^{-1}. A typical model smearing length scale is therefore about 50 km, close to the dimensions of the GEOS-Chem grid, which range from 68×56 km^2 to 74×56 km^2.

[25] To ensure that the impact of spatial smearing is minimal, we adopt a similar approach to the work of *Marais et al.* [2012], whereby for each scenario we run an additional simulation with isoprene emissions increased by a uniform 25%. We then identify grid squares where $\Delta S = \Delta\Omega'_v/\Delta E'_{\mathrm{isop}}$ is within 1300–1800 s, and fit a linear regression between the unperturbed isoprene emissions and HCHO columns at only these locations; grid cells with slopes outside this range are discarded. The slope S multiplied by the HCHO column loss rate constant should approximately equal the HCHO yield [*Palmer et al.*, 2003]. Thus, using a mean HCHO column lifetime of 2.5 h applied to ΔS slopes of 1300 to 1800 s correspond to yields of 0.14 to 0.2 per C, consistent with yields calculated in the photochemical box-model (cf. Figure 1 and Table 3) and simulated GEOS-Chem boundary layer NO_x. Grid cells with ΔS values outside the defined range indicate regions where model HCHO yields are excessively high or low, and use of a transfer function is not reliable. We find that the ΔS filtering typically avoids areas of very low isoprene emissions, where HCHO contributions to the vertical column come from other sources or regions.

[26] Figure 2, which shows the relationship between the model isoprene emissions and HCHO columns for October 2006 (PCEEA scenario), illustrates how this ΔS filtering improves the model correlations from 0.65 to 0.97 for SCIAMACHY, and 0.66 to 0.95 for OMI. Over the full ensemble, the correlation range increases to 0.82–0.99, with mean correlations of 0.93 for SCIAMACHY and 0.91 for OMI (see Table 4). The strong linear dependence is consistent with isoprene oxidation controlling HCHO column variability where smearing is negligible. Furthermore, using values from our default PCEEA scenario, we explicitly calculate median displacement lengths of 15–44 km ($\overline{L_d} \sim 17$ km) and estimate median smearing lengths of 19–57 km ($\overline{L_s} \sim 34$ km) at locations meeting the ΔS criteria, which are within the dimensions of the GEOS-Chem grid cells, thus providing credibility to this approach. Occurrence of fast tropospheric winds (>50 km hr^{-1}), especially at grid cells discarded by the ΔS filtering, contributes to smearing distances exceeding 100 km, which reduces the influence of local emissions on the HCHO column.

[27] Figure 3, which shows the seasonal variation in the model correlations and regression parameters over the ensemble, illustrates that there are clear differences between the scenarios reflecting the model uncertainty in its simulation of isoprene emissions and tropospheric oxidation chemistry. Simulations that use MEGAN emissions tend to show very similar trends, in contrast to the two LPJ-GUESS scenarios. For example, the LPJ-G5 and LPJ-CRU regression slopes are strikingly higher at the time of SCIAMACHY overpass, and the LPJ-G5 correlations are noticeably worse for OMI. Since simulated boundary layer NO_x levels are similar over the ensemble, the regression differences most likely reflect the model response to seasonal variations in the respective isoprene emission inventories.

5. Results

5.1. Top-Down Isoprene Emissions

[28] Table 4 summarizes the top-down isoprene emissions inferred from the retrieved SCIAMACHY and OMI HCHO vertical columns, and as an example, we show in Figure 4 top-down isoprene emissions from OMI, derived using regression parameters from our default PCEEA scenario (described in Table 1). Figure 4 demonstrates the fire- and ΔS-screening limits of the coverage over the domain; often, emissions are only calculated at <20% of land grid cells with many regions undetermined. It is therefore difficult to establish distinct patterns in the top-down emissions

over the entire Amazon Basin. Nevertheless, our results indicate the satellite HCHO data help constrain isoprene emissions at these locations. For example, over the ensemble, the a priori emissions for SCIAMACHY range from 27–61 Tg C with a mean and 1 standard deviation of 47 ± 9 Tg C. For OMI, the a priori emissions cover 45–104 Tg C with a mean of 62 ± 13 Tg C. The subsequent posterior top-down emissions cover a much smaller range of 31–38 Tg C for SCIAMACHY (mean 34 ± 2 Tg C), and 28–38 Tg C for OMI (mean 32 ± 2 Tg C), respectively, thereby reducing the overall uncertainty in isoprene emissions from this region within this model-retrieval framework.

[29] Although some scenarios use the same bottom-up inventory, their a priori emissions differ due to filtering ΔS into its defined range. Thus, a more suitable diagnostic to compare the different scenarios is the relative difference in the monthly emission totals, hereafter referred to as δE_{MT}, given by

$$\delta E_{\mathrm{MT}} = 100\% \times \frac{\text{Posterior - Prior}}{\text{Prior}} \quad (5)$$

Overall, mean values of δE_{MT} are –24 ± 16% for SCIAMACHY and –48±10% for OMI, indicating that, in general, the bottom-up isoprene emissions need to be significantly reduced to be consistent with the HCHO column observations. The top-down isoprene emissions inferred from OMI are broadly consistent with the study of *Marais et al.* [2012], who found that OMI-derived emissions were on average 43% lower than MEGAN over the central African tropical rainforest.

[30] Figure 3 demonstrates that δE_{MT} has a distinct seasonal trend with the posterior emissions much lower than the prior during May–June, a transitional period between the wet and dry seasons when isoprene fluxes may be unusually low [*Barkley et al.*, 2008, 2009]. Apart from the LPJ-GUESS scenarios, the top-down emissions derived from SCIAMACHY deviate least from the prior emissions during Nov–Dec and Feb–Apr. The OMI derived estimates are substantially lower than the prior throughout the year. Top-down emissions derived using the LPJ-GUESS scenarios are notably different, especially those from SCIAMACHY, which indicate that the bottom-up emissions need to be increased for the majority of the year. For OMI, the LPJ-GUESS top-down estimates are closest to their prior totals during the dry season, but are also lower than the bottom-up emissions at other times.

[31] We find that δE_{MT} is not greatly affected by the use of a different boundary layer mixing scheme (scenario BL), slower oxygenated VOC deposition rates (SLOWDEP), a shorter model time step (CHEMT), or the fast photolysis of hydroperoxy aldehydes (HPALD). We also find the AMF sensitivity scenarios do not greatly affect the top-down emissions, causing differences to the PCEEA scenario of less than 10% for either instrument. The explicit treatment of hydroperoxy aldehydes in the chemical scheme (scenario LIM0) moderately affects OMI-derived emissions (δE_{MT} is –67% compared to –51% in the PCEEA scenario) but not SCIAMACHY, probably reflecting the more active photochemistry, which occurs around midday. However, in general, we find it is the choice of isoprene inventory which largely determines the value of δE_{MT} (see columns 3–5 of Table 4).

5.2. Uncertainties

[32] We estimate the error on the top-down emissions (ϵ_E) by applying the uncertainties associated with the HCHO vertical columns (ϵ_v), and the model regression slopes (ϵ_S) and intercepts (ϵ_B), to equation (3) using error propagation:

$$\epsilon_E^2 = \frac{1}{S^2}\epsilon_v^2 + \left(\frac{B-\Omega_v}{S^2}\right)^2 \epsilon_S^2 + \frac{1}{S^2}\epsilon_B^2 + \frac{2}{S}\left(\frac{\Omega_v - B}{S^2}\right)\mathrm{cov(S,B)} \quad (6)$$

where the last term accounts for covariance between the model slopes (S) and intercepts (B). Using equation (6), we calculate monthly median uncertainties on the top-down emissions of typically 60–260% for SCIAMACHY, and 10–90% for OMI. The lower uncertainties associated with OMI are consistent with its much higher number of soundings reducing random errors in the HCHO column retrieval. Uncertainties are greatest during April–June when the inferred top-down isoprene emissions are very low, and lowest during August–November when emissions are highest. Given the large uncertainties in tropical isoprene oxidation chemistry, and known limitations of the mass-balance approach [*Turner et al.*, 2012], we acknowledge these error estimates are probably optimistic.

6. Sensitivity Analysis

[33] In this section we further explore the uncertainties by examining the sensitivity of the top-down estimates to four key aspects: (1) the fire-screening technique, (2) choice of grid resolution, (3) ΔS spatial filtering, and (4) the HCHO vertical column product. Here we use the change in δE_{MT} for each scenario to diagnose the sensitivity to a particular assumption, i.e.,

$$\Delta E_{\mathrm{MT}} = (\delta E_{\mathrm{MT}})_{\text{Sensitivity Test}} - (\delta E_{\mathrm{MT}})_{\text{Default Settings}} \quad (7)$$

where the default settings are based on screening of fires daily and the use of locations where ΔS is within 1300–1800 s, as outlined in sections 4.2 and 4.3. Figure 5 shows the seasonal variation in ΔE_{MT} resulting from these additional tests.

6.1. Sensitivity to Fire Filtering

[34] To assess whether the top-down emissions estimates are likely to be affected by our fire-screening method we additionally test three further fire-filtering techniques. First, we run a stricter daily filter discarding observations falling within ±2 grid cells of an active fire. Second, we construct eight day fire masks using binned AATSR data and the eight day MODIS Climate Modeling Grid (CMG) products MYD14C8H and MOD14C8H (0.5° × 0.5° resolution), remapped to the nested grid. The CMG products are statistical summaries of each eight day period and benefit from improved fire classification [*Giglio et al.*, 2006]. Again, a SCIAMACHY and OMI HCHO column observation is discarded if a fire occurs in either the grid cells in which it falls or if in those immediately adjacent (±1 grid cells) of the concurrent or preceding eight day period. Third, we construct monthly fire masks using binned AATSR data and the remapped monthly MODIS CMG products MYD14CMH and MOD14CMH, only discarding HCHO column observations if a fire occurs in a coincident grid cell of the same month.

Table 3. Time Dependent HCHO Yields per Carbon From the Oxidation of Isoprene[a]

	Cumulative HCHO Yield Per C From 1 ppbv of Isoprene Released at 09:00 Local Time			Cumulative HCHO Yield Per C From 1 ppbv of Isoprene Released at 12:00 Local Time		
NO_x [ppbv]	Yield at 11:00	Yield After 24 h	Ultimate Yield	Yield at 15:00	Yield After 24 h	Ultimate Yield
1.0	0.25	0.39	0.43	0.32	0.39	0.43
0.5	0.23	0.38	0.42	0.30	0.38	0.42
0.1	0.13	0.30	0.39	0.19	0.29	0.38
0.05	0.11	0.26	0.37	0.17	0.26	0.36
0.01	0.08	0.21	0.32	0.14	0.21	0.32

[a]The GEOS-Chem HCHO yields are calculated using 0-d photochemical box-model, as described in *Barkley et al.* [2011] and are appropriate to the Amazon environment. The box-model is initialized with 1 ppbv of isoprene, which is allowed to decay and 100 ppbv of CO and 25 ppbv of ozone, respectively, which are held constant throughout the simulation. Different NO_x regimes are simulated by fixing its absolute mixing ratio, although individually, the relative concentrations of NO and NO_2 are allowed to vary over the course of the day. We assume surface conditions and sea-level pressure and hold water-vapor constant at 25,000 ppmv.

[35] Figure 5 shows that the impact of the fire-filtering method is generally minor, causing additional changes in δE_{MT} of about $\pm$10%. The greatest differences typically occur in the dry season and is more evident for SCIAMACHY owing to its less frequent sampling. Use of the eight day MODIS CMG products produces the greatest changes ($\Delta E_{MT} \sim$ 20–30%), as a high percentage of grid cells are discarded (sometimes over 80%) and spatial coverage is particularly poor. In the case of the eight day and monthly filtering, the model correlations are typically weaker, being 0.72–0.98 and 0.79–0.99, respectively, as compared with 0.84–0.99 when using the default biomass burning screening.

6.2. Sensitivity to Grid Resolution (Spatial Aggregation)

[36] As the native grid resolution is close to the limit of the smearing and displacement lengths, we repeat our analysis but with the satellite data and model output degraded to grid resolutions of 1.33° × 1.0° and 2.66° × 2.0°. At these coarser grid resolutions the dimensions of each grid cell exceed 100 km, greater than the typical smearing (19–57 km) and displacement (15–44 km) lengths calculated in section 4.3. Figure 5 shows that at 1.33° × 1.0° the effect of spatial aggregation is minimal on the emissions inferred from SCIAMACHY, but generally lowers the posterior emissions of OMI by up to an additional 15%. The change in δE_{MT} is larger at 2.66° × 2.0°, with ΔE_{MT} being within about $\pm$10% for SCIAMACHY, and 0 to –20% for OMI. However, model correlations are noticeably worse as we degrade the data to coarser resolutions. In particular, the minimum correlations are now as low as 0.61, thus, confidence in the relationship between the model isoprene emissions and HCHO columns, and therefore the top-down estimates, is diminished.

6.3. Sensitivity to Regression Slopes

[37] As shown in Figure 4, filtering ΔS into a tight range compromises the spatial coverage of the top-down emissions. We therefore repeat our analysis, but this time separately constraining ΔS within 1000–2000 s and 1000–2500 s (i.e., corresponding to HCHO yields of 0.11–0.22 and 0.11–0.28 per C) to potentially increase the number of locations where top-down emissions can be inferred. Despite increased coverage of the domain and weaker model correlations, δE_{MT} changes very little with $\Delta E_{MT} \sim \pm$5% (not shown).

6.4. Sensitivity to HCHO Columns

[38] Our choice of reference sector correction and use of a priori model data in the AMF calculation, results in HCHO vertical columns that differ from those in the standard satellite products. The SCIAMACHY and OMI HCHO columns used in this study are on average about 15% higher and 10% lower, respectively, when screening for fires daily. We therefore recalculate the top-down emissions with the original HCHO vertical columns using the data as is, since averaging kernels for OMI are not currently available. This results in lower posterior emissions for SCIAMACHY (from 31–38 Tg C to 25–29 Tg C), and higher posterior emissions for OMI (28–38 Tg C to 35–44 Tg C). Figure 5 demonstrates that the magnitude of the inferred top-down isoprene emissions are most sensitive to the HCHO column data itself, rather than different assumptions in fire screening, regression slopes, or grid resolution, since the resulting ΔE_{MT} is far greater than from any other sensitivity test. This may seem intuitively obvious, but it is important to quantify this uncertainty since studies which use SCIAMACHY or OMI HCHO data, often apply different reference sector corrections and/or recalculate the AMFs themselves [e.g., *Millet et al.*, 2008; *Gonzi et al.*, 2011; *Barkley et al.*, 2012; *Marais et al.*, 2012].

7. Building and Evaluating a Complete Top-Down Emission Map

[39] A more complete picture of the top-down isoprene emissions is required if we are to assess whether the inferred estimates improve the GEOS-Chem simulation of HCHO over the Amazon. To build a continuous distribution of the top-down emissions, we therefore now relax our strict application of the regression parameters determined using ΔS, by applying them to every fire-free grid square. We then fill in the remaining undetermined grid cells by scaling the prior emissions at these locations by δE_{MT}, as done similarly in

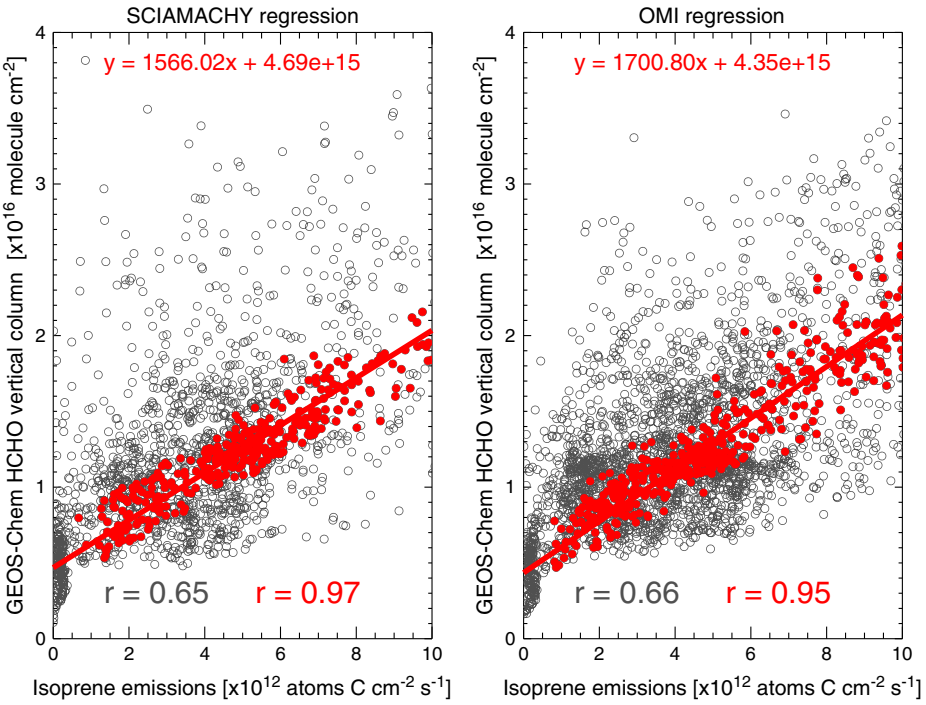

Figure 2. Relationship between GEOS-Chem isoprene emissions and HCHO vertical columns for October 2006 at (left) 9–11 LT and (right) 12–15 LT corresponding to the overpasses of SCIAMACHY and OMI, respectively, taken from the PCEEA scenario (see Table 1). Model data has been sampled along each instrument's orbital track and averaged on to the $0.667° \times 0.5°$ GEOS-Chem grid using observations with a cloud faction $\leq$40%. Grey open circles correspond to all land grid cells screened daily for fires. Red filled circles indicate grid cells where ΔS is within 1300–1800 s, with the reduced major axis linear fit to these points (see section 4.3). The Pearson correlation coefficient r is shown inset.

Barkley et al. [2008]. We acknowledge that some locations might be affected by spatial smearing or have low HCHO production rates thereby introducing some degree of uncertainty, but for the purpose of this exercise, we have to assume these effects are small.

[40] Table 5 shows the effect this filling-in procedure has on the annual totals. Despite applying the regression slope to every fire-screened grid square, the relative differences in δE_{MT} only change by a few percent, indicating that this step does not greatly affect the scaling required to bring prior emissions into alignment with posterior estimates. Similarly, by then filling in all the cloudy grid squares or those grid squares where emissions are undetermined (using δE_{MT}), we can now directly compare one scenario to another; though these estimates should be trusted less as we have to fill in with the prior emissions; 2–45% of GEOS-Chem grid cells are filled in this way. Even so, as in section 5, we find that the top-down emissions are largely independent of choice of boundary-layer mixing scheme, fast/slow dry deposition, the treatment of hydroxyperoxy aldehydes, chemical time step or surface reflectance in the AMF calculation. Instead, the top-down emissions are most sensitive to errors in cloud top-pressure and fractional coverage (up to 10% difference) and use of lower isoprene emissions from the MULLER scenario or either of the LPJ-GUESS scenarios (10–20% differences). We find over the ensemble the isoprene emission range (or uncertainty) decreases from 193–393 Tg C (mean 345 ± 65 Tg C) to 217–288 Tg C (mean 261 ± 18 Tg C), and from 201–442 Tg C (mean 371 ± 72 Tg C) to 149–195 Tg C (mean 171 ± 13 Tg C) through use of the SCIAMACHY and OMI HCHO data, respectively.

[41] Figure 6 shows complete maps of the a priori and posterior emissions corresponding to the PCEEA and LPJ-G5 scenarios. Despite two different sets of a priori emissions, we find that outside the dry season (i.e., Jan–Jun) the top-down emissions derived from SCIAMACHY and OMI generally agree in spatial distribution and amount for each instrument, respectively. For both instruments, the biggest differences between the inferred top-down emissions from each scenario occur in the dry season; emissions derived from the PCEEA scenario are greater than those derived from the LPJ-G5 scenario. Lack of coverage in these months probably contributes to this disagreement. An issue with SCIAMACHY is that over the SAA affected area, the top-down estimates are solely based on the scaled a priori emissions, and this is where top-down emissions tend to show the most disagreement between different scenarios. The greatest emissions occur along the Brazilian border with Peru and Bolivia, and from the Selvas rainforest plains, with typical rates of about 5–15 atoms C cm^{-2} s^{-1} (i.e., 4–12 mg isoprene m^{-2} h^{-1}). Inspection of the top-down emission inferred from other scenarios also demonstrate these characteristics. Scenarios that use MEGAN HYBRID or PCEEA emissions result in top-down isoprene emission distributions with very similar spatial features (see Figures S1 and S2 in the supporting information), and that have monthly totals typically within 4–6 Tg C of one another during the dry season, and 1–4 Tg C otherwise. However, top-down emissions

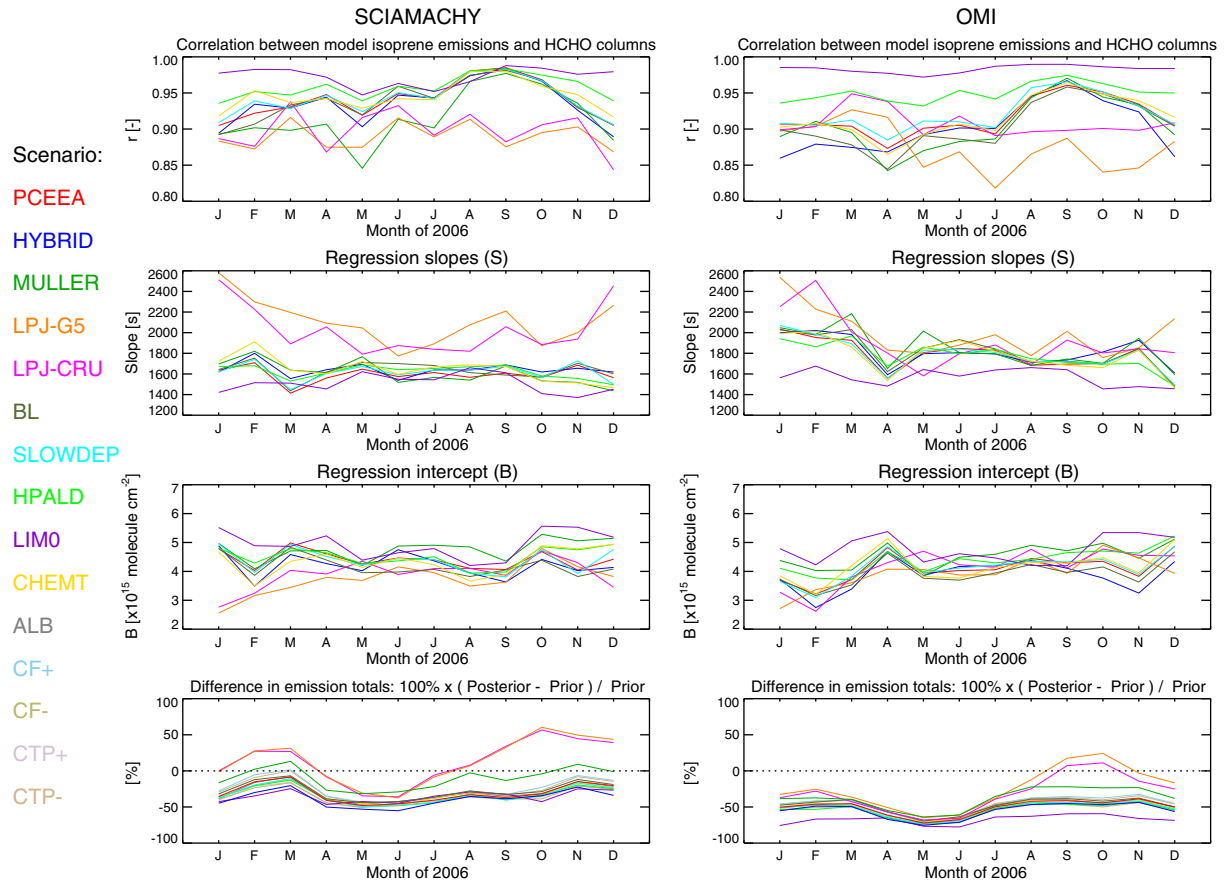

Figure 3. Seasonal variation of model correlations, regression slopes and intercept, and the relative differences in the monthly top-down emission totals (δE_{MT}; equation (5)), for each ensemble scenario and corresponding to the values presented in Table 4.

derived from the LPJ-CRU scenario exhibit differing spatial patterns to those based on the unscaled MEGAN algorithms (Figure S3).

[42] We run GEOS-Chem with the top-down emissions derived using the default PCEEA scenario in three ways: (1) we adjust the model emissions at 9–11 LT and 12–15 LT using corresponding scaling factors from the SCIAMACHY and OMI top-down emissions (leaving the bottom-up emissions outside these time periods unchanged) or we separately adjust the model emissions at all time steps using scaling factors determined from (2) SCIAMACHY or (3) OMI alone. We find in all cases that the agreement between the model and observations is improved. However, examination of the HCHO column biases and correlations indicate that the best model agreement to SCIAMACHY is obtained using method (1), but only marginally when compared with method (2). This effect might result from OMI's more frequent sampling offering additional information in areas not covered by SCIAMACHY (despite the different observing times). For OMI the best model agreement is found using approach (3).

[43] Figure 7 shows the satellite and the model HCHO columns, obtained by using the top-down emissions (the AMFs are recalculated in each instance). We find that for every month, the bias between the model and observations is decreased and the correlations increased. The annual normalized mean bias decreases from 68% to 22% for OMI, and from 24% to –1% for SCIAMACHY. The mean correlations improve from 0.52 to 0.66 for OMI and from 0.59 to 0.68 for SCIAMACHY. Use of the top-down emissions therefore clearly improves the GEOS-Chem simulation of HCHO although it does not completely remove the model bias with respect to the OMI data. We additionally run GEOS-Chem using top-down isoprene emissions inferred from the LPJ-G5 scenario. Again, we find that the agreement between GEOS-Chem and the satellite data is generally improved, the only exception being the model bias with respect to SCIAMACHY, if OMI top-down emissions are used. For example, the bias and correlations for SCIAMACHY improve from –3% to 1% and 0.60 to 0.67, when using approach (2), and for OMI from 31% to 17%, and 0.62 to 0.72 when using approach (3). Therefore, irrespective of the two scenarios, the inferred top-down isoprene emissions generally improve GEOS-Chem's simulation of HCHO with respect to the SCIAMACHY and OMI measurements.

[44] If the satellite estimates are credible, we may make several general conclusions about the prior inventories: (1) MEGAN's spatial distribution agrees reasonably with the satellite emissions, but the prior estimates need to be scaled significantly downward to match in magnitude; that said, the very high predicted emissions along the Brazilian border with Peru and Bolivia are clearly not consistent with satellite data; (2) the LPJ-GUESS emissions are closer in magnitude

Table 4. Top-Down Isoprene Emissions Estimates Derived From SCIAMACHY and OMI

	Summary of Isoprene Emissions[a]					Summary of Model Regression[b]								
	Annual Totals (Tg C)		δE_{MT} (%)[c]			Correlation r (-)			S (s)			B ($\times 10^{15}$ Molec cm^{-2})		
	Prior	Posterior	Mean	Max	Min	Mean	Max	Min	Mean	Max	Min	Mean	Max	Min
						SCIAMACHY								
PCEEA	50	34	–31	–9	–48	0.94	0.98	0.90	1595	1709	1414	4.40	4.98	4.03
HYBRID	61	37	–39	–20	–55	0.94	0.98	0.89	1642	1800	1538	4.21	4.89	3.49
MULLER	38	34	–10	13	–32	0.92	0.98	0.85	1610	1820	1436	4.76	5.28	4.09
LPJ-G5	27	31	14	60	–37	0.89	0.92	0.87	2109	2581	1774	3.72	4.79	2.55
LPJ-CRU	29	33	13	57	–36	0.90	0.94	0.84	2029	2513	1791	3.89	4.71	2.76
BL	47	34	–28	–7	–44	0.94	0.98	0.89	1635	1753	1437	4.17	4.83	3.82
SLOWDEP	52	34	–33	–11	–50	0.94	0.98	0.91	1618	1742	1449	4.38	4.95	3.81
HPALD	54	36	–33	–13	–49	0.96	0.98	0.94	1622	1688	1495	4.51	4.93	3.94
LIM0	59	38	–35	–25	–46	0.97	0.99	0.95	1510	1660	1371	4.93	5.56	4.20
CHEMT	47	32	–31	–11	–48	0.95	0.98	0.92	1644	1912	1466	4.34	4.94	3.50
ALB	50	34	–30	–8	–46	0.94	0.98	0.90	1595	1709	1414	4.40	4.98	4.03
CF+	50	37	–25	2	–43	0.94	0.98	0.90	1595	1709	1414	4.40	4.98	4.03
CF–	50	32	–35	–17	–50	0.94	0.98	0.90	1595	1709	1414	4.40	4.98	4.03
CTP+	50	32	–35	–16	–51	0.94	0.98	0.90	1595	1709	1414	4.40	4.98	4.03
CTP–	50	36	–26	0	–45	0.94	0.98	0.90	1595	1709	1414	4.40	4.98	4.03
						Ensemble[d]								
Max	61	38	14	60	–32	0.97	0.99	0.95	2109	2581	1791	4.93	5.56	4.20
Min	27	31	–39	–25	–55	0.89	0.92	0.84	1510	1660	1371	3.72	4.71	2.55
Mean	47	34	–24	0	–45	0.94	0.98	0.90	1665	1848	1482	4.36	4.99	3.76
$\pm 1\sigma$	9	2	16	25	6	0.02	0.02	0.03	167	290	128	0.29	0.20	0.49
						OMI								
PCEEA	61	30	–51	–39	–72	0.92	0.96	0.87	1780	2034	1480	4.11	4.87	3.22
HYBRID	71	32	–55	–44	–75	0.90	0.97	0.86	1816	2020	1593	3.88	4.69	2.75
MULLER	45	28	–38	–22	–64	0.91	0.97	0.84	1846	2184	1593	4.54	5.12	3.84
LPJ-G5	46	35	–25	24	–65	0.88	0.93	0.82	1992	2537	1758	3.94	4.91	2.71
LPJ-CRU	56	38	–32	11	–68	0.91	0.95	0.89	1908	2507	1581	4.15	4.77	2.62
BL	58	30	–48	–38	–69	0.90	0.96	0.84	1811	2030	1473	3.93	4.68	3.16
SLOWDEP	63	31	–52	–42	–74	0.92	0.97	0.88	1787	2070	1495	4.13	4.87	3.10
HPALD	73	34	–54	–42	–73	0.95	0.97	0.93	1774	1969	1482	4.39	5.23	3.71
LIM0	104	34	–67	–59	–78	0.98	0.99	0.97	1568	1677	1455	4.76	5.38	4.19
CHEMT	61	31	–51	–40	–71	0.92	0.96	0.86	1780	2012	1464	4.19	5.13	3.20
ALB	61	31	–50	–40	–72	0.92	0.96	0.87	1780	2034	1480	4.11	4.87	3.22
CF+	61	33	–47	–33	–71	0.92	0.96	0.87	1780	2034	1480	4.11	4.87	3.22
CF–	61	28	–54	–44	–73	0.92	0.96	0.87	1780	2034	1480	4.11	4.87	3.22
CTP+	61	28	–55	–43	–75	0.92	0.96	0.87	1780	2034	1480	4.11	4.87	3.22
CTP–	61	33	–47	–34	–70	0.92	0.96	0.87	1780	2034	1480	4.11	4.87	3.22
						Ensemble[d]								
Max	104	38	–25	24	–64	0.98	0.99	0.97	1992	2537	1758	4.76	5.38	4.19
Min	45	28	–67	–59	–78	0.88	0.93	0.82	1568	1677	1455	3.88	4.68	2.62
Mean	62	31	–48	–32	–71	0.92	0.96	0.88	1797	2080	1518	4.17	4.93	3.24
$\pm 1\sigma$	13	2	10	21	3	0.02	0.01	0.04	87	207	81	0.23	0.20	0.42

[a]The emission estimates are based on the daily screening of fires and the use of grid cells where ΔS is within 1300–1800 s (see sections 4.2 and 4.3).
[b]Regression between the model isoprene emissions and HCHO vertical columns (equation (3)); S and B are the gradient and intercept of the reduced major axis fit which allows for errors in both parameters [*Hirsch and Gilroy*, 1984], and r is the Pearson correlation coefficient.
[c]The percent differences of the monthly emission totals, i.e., 100% × (posterior-prior)/prior (see equation (5)).
[d]Summary over the ensemble.

with posterior estimates, but in some months, the distribution of the emissions is wrong (see e.g., the high LPJ-CRU emissions in the southeast during March–April, as shown in Figure S3); (3) all inventories fail to predict the very low emissions detected during April–June; (4) the improvement in the GEOS-Chem HCHO column simulation is greater using top-down emissions inferred from the PCEEA rather than LPJ-G5 scenario (i.e., the prior LPJ-G5 emissions produced the more realistic original simulation); (5) the model agreement to the satellite data is marginally better using satellite emissions derived from the LPJ-G5 scenario. This may suggest that use of the LPJ-G5 emissions is preferential over the PCEEA scenario, but as discussed in *Barkley et al.* [2011], it possible that the much lower emissions from LPJ-GUESS are potentially compensating for other GEOS-Chem uncertainties (e.g., chemistry).

8. Comparison of SCIAMACHY and OMI Top-Down Emissions

[45] To directly compare the estimates from SCIAMACHY and OMI, we scale the local time emissions to monthly mean estimates using their corresponding model relationship and recalculate the annual totals (see Table 5), assuming that the model accurately simulates the isoprene emission diurnal cycle. Direct comparison of the top-down emissions also assumes that the model transfer functions are appropriate for the satellite overpass times, i.e., GEOS-Chem's entire diurnal simulation is accurate. We find that the SCIAMACHY top-down estimates are nearly twice those derived from OMI, even though the HCHO columns from the two instruments differ on average by 25% (relative to SCIAMACHY); the top-down isoprene emissions derived

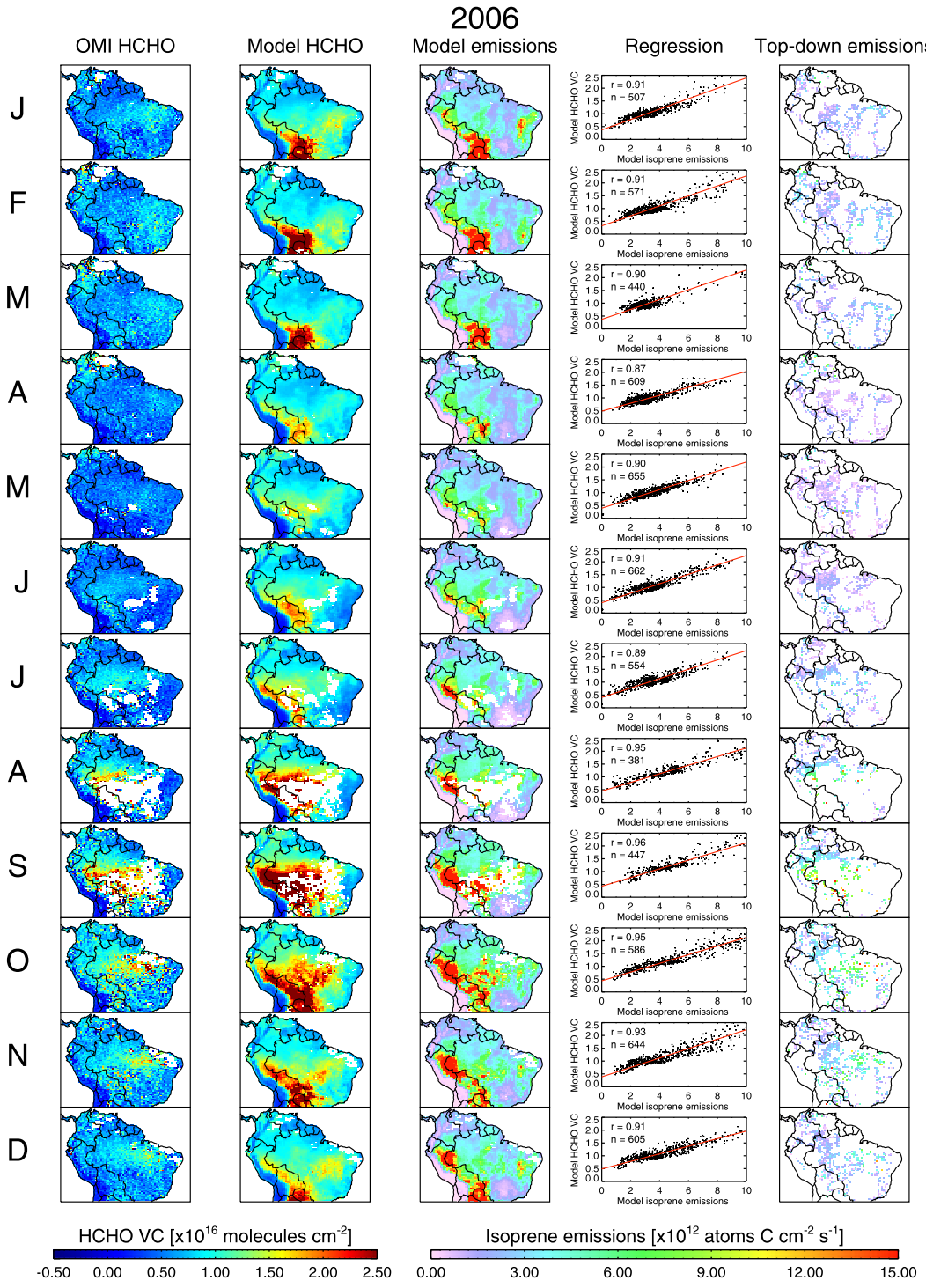

Figure 4. Monthly mean HCHO columns for 2006 corresponding to 12–15 LT, as (first column) observed by OMI and (second column) simulated by GEOS-Chem, using (third column) isoprene emissions from the PCEEA scenario. The OMI data have been averaged onto the nested 0.667°×0.5° grid using observations with cloud cover ≤40% and screened daily for biomass burning. The model data have been sampled at the same times and locations as the OMI observations; white pixels indicate missing data. (fourth column) The model regression using locations where ΔS is within 1300–1800 s, with the number of grid cells and correlation shown inset. The final column shows the top-down emissions inferred from the OMI HCHO column data using the linear regression.

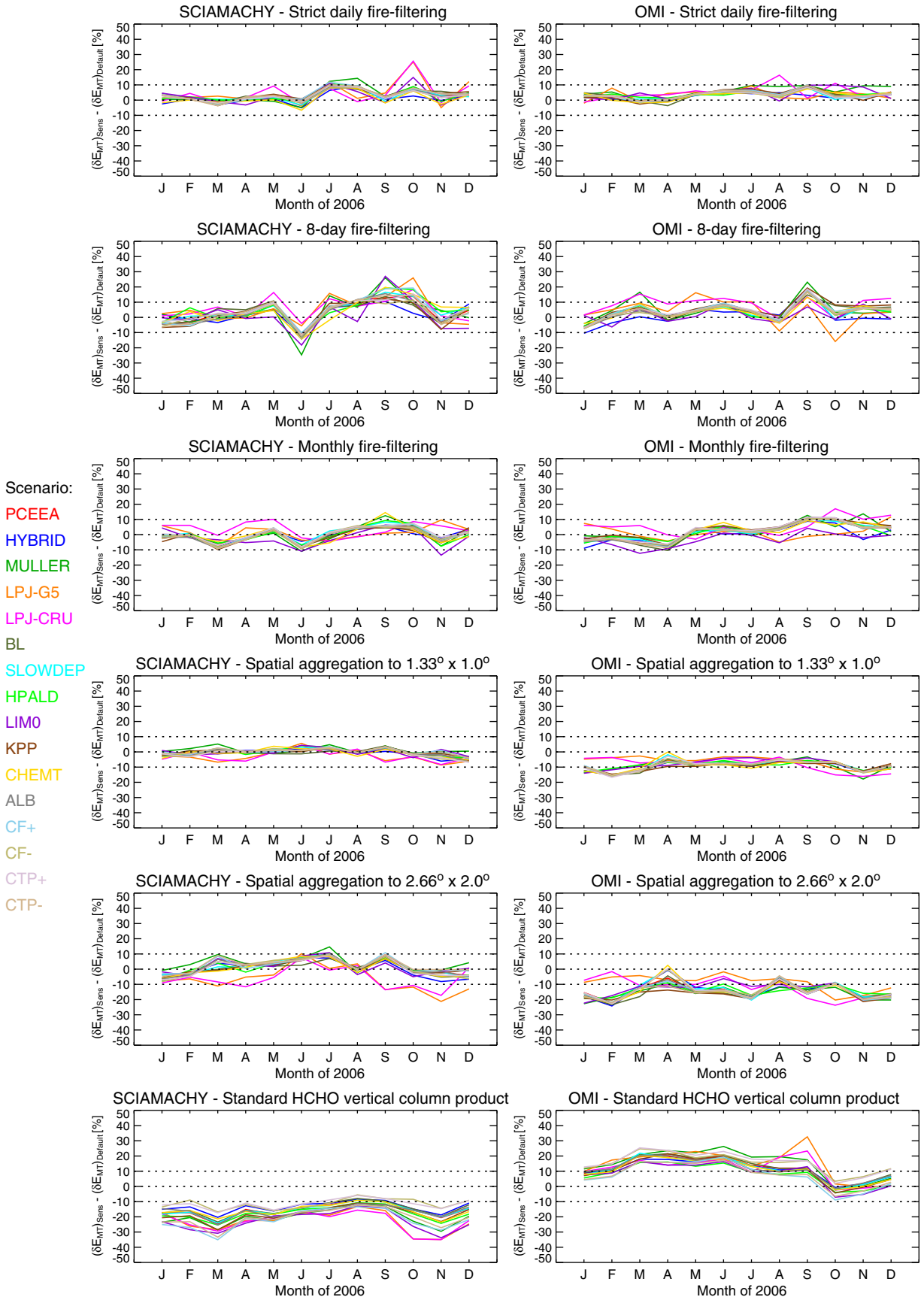

Figure 5. The seasonal change in δE_{MT} for each ensemble scenario arising from the different sensitivity tests discussed in section 6 (see equation (5)).

Table 5. Annual Summary of Complete SCIAMACHY and OMI Top-Down Isoprene Emission Maps

	Local Time Emissions							Scaled to Monthly Means	
	Fire-Screened Grid Cells[a]					All Land Grid Cells[b]		All Land Grid Cells[c]	
	Annual Totals (Tg C)		δE_{MT} (%)[d]			Annual Totals (Tg C)		Annual Totals (Tg C)	
	Prior	Posterior	Mean	Max	Min	Prior	Posterior	Prior	Posterior
					SCIAMACHY				
PCEEA	234	162	–30	–14	–48	377	265	135	93
HYBRID	253	163	–35	–18	–53	393	259	148	95
MULLER	161	150	–6	15	–31	250	236	94	87
LPJ–G5	125	139	13	60	–19	193	217	73	82
LPJ–CRU	130	141	11	57	–20	228	254	88	97
BL	234	164	–30	–13	–49	377	268	135	93
SLOWDEP	234	162	–31	–14	–49	377	265	135	92
HPALD	234	163	–30	–15	–47	377	267	135	93
LIM0	234	175	–25	–13	–43	377	286	135	100
CHEMT	213	161	–24	–6	–45	344	264	135	101
ALB	234	164	–29	–11	–49	377	269	135	94
CF+	234	176	–25	–9	–42	377	288	135	100
CF–	234	155	–33	–15	–50	377	254	135	89
CTP+	234	152	–35	–17	–52	377	249	135	87
CTP–	234	175	–25	–9	–43	377	285	135	99
					Ensemble				
Max	253	176	13	60	–19	393	288	148	101
Min	125	139	–35	–18	–53	193	217	73	82
Mean	214	160	–22	–1	–42	345	261	125	93
$\pm 1\sigma$	40	11	15	25	10	65	18	21	5
					OMI				
PCEEA	354	149	–58	–38	–72	399	173	135	56
HYBRID	373	150	–60	–40	–75	418	173	148	59
MULLER	237	128	–46	–14	–65	265	149	94	51
LPJ–G5	183	136	–24	22	–62	201	152	73	55
LPJ–CRU	217	140	–34	5	–66	242	159	88	58
BL	354	152	–58	–36	–71	399	176	135	57
SLOWDEP	354	148	–59	–39	–73	399	173	135	56
HPALD	354	148	–59	–39	–73	399	173	135	56
LIM0	354	167	–53	–30	–68	399	195	135	63
CHEMT	374	148	–61	–40	–72	442	173	135	53
ALB	354	150	–58	–37	–71	399	175	135	56
CF+	354	162	–55	–32	–71	399	188	135	61
CF–	354	139	–61	–43	–73	399	161	135	52
CTP+	354	136	–62	–43	–75	399	158	135	51
CTP–	354	162	–55	–33	–69	399	188	135	61
					Ensemble				
Max	374	167	–24	22	–62	442	195	148	63
Min	183	128	–62	–43	–75	201	149	73	51
Mean	328	147	–53	–29	–70	371	171	125	56
$\pm 1\sigma$	61	10	10	18	3	72	13	21	3

[a]Here the regression parameters determined from the ΔS filtering (section 4.3) are applied to all grid cells which have been screened for biomass burning daily and contain HCHO column observations with cloud fractional coverage $\leq 40\%$ (see section 7).
[b]As above, but with the remaining undetermined grid cells filled in with the scaled prior bottom-up emissions (see section 7).
[c]The local-time (LT) monthly emission totals corresponding to each satellite overpass are scaled to monthly mean emission totals (MM) using the following relationship: $MM_{Satellite} = LT_{Satellite} \times (MM_{Model}/LT_{Model})$.
[d]The percent differences of the monthly emission totals, i.e., 100% × (posterior-prior)/prior (see equation (5)).

from SCIAMACHY are 82–101 Tg C (mean 93 ± 5 Tg C) compared to 51–63 Tg C (mean 56 ± 3 Tg C) inferred from OMI (see Table 5). We find sampling the OMI data in the same way as SCIAMACHY cannot explain the difference in the inferred top-down emissions, nor can potential uncertainties in the respective cloud products.

[46] Unfortunately, there are not any in situ measurements to validate the SCIAMACHY and OMI HCHO columns during our study year to establish a potential retrieval bias. However, aircraft measurements of HCHO mixing ratios made during the GABRIEL campaign [*Stickler et al.*, 2007], conducted in October 2005 over the Guyanas, can provide a limited assessment of the OMI data; validation of SCIAMACHY measurements could not be made owing to the instrument's less frequent sampling. During the GABRIEL campaign, flights were performed over both land and ocean, sampling the boundary layer and free troposphere (approximately 300 m–10 km). For the comparison to OMI, only aircraft observations within 12–15 LT were used; only valid data for 5,7,8, 11, and 15 October existed. The HCHO observations were binned into 50 hPa bins extending from surface pressure (taken from GEOS-Chem) to construct a mean HCHO profile over this period, and thus a vertical column. Only observations to about 8 km existed, no extrapolation was performed beyond this altitude. Hence, the calculated aircraft HCHO vertical column,

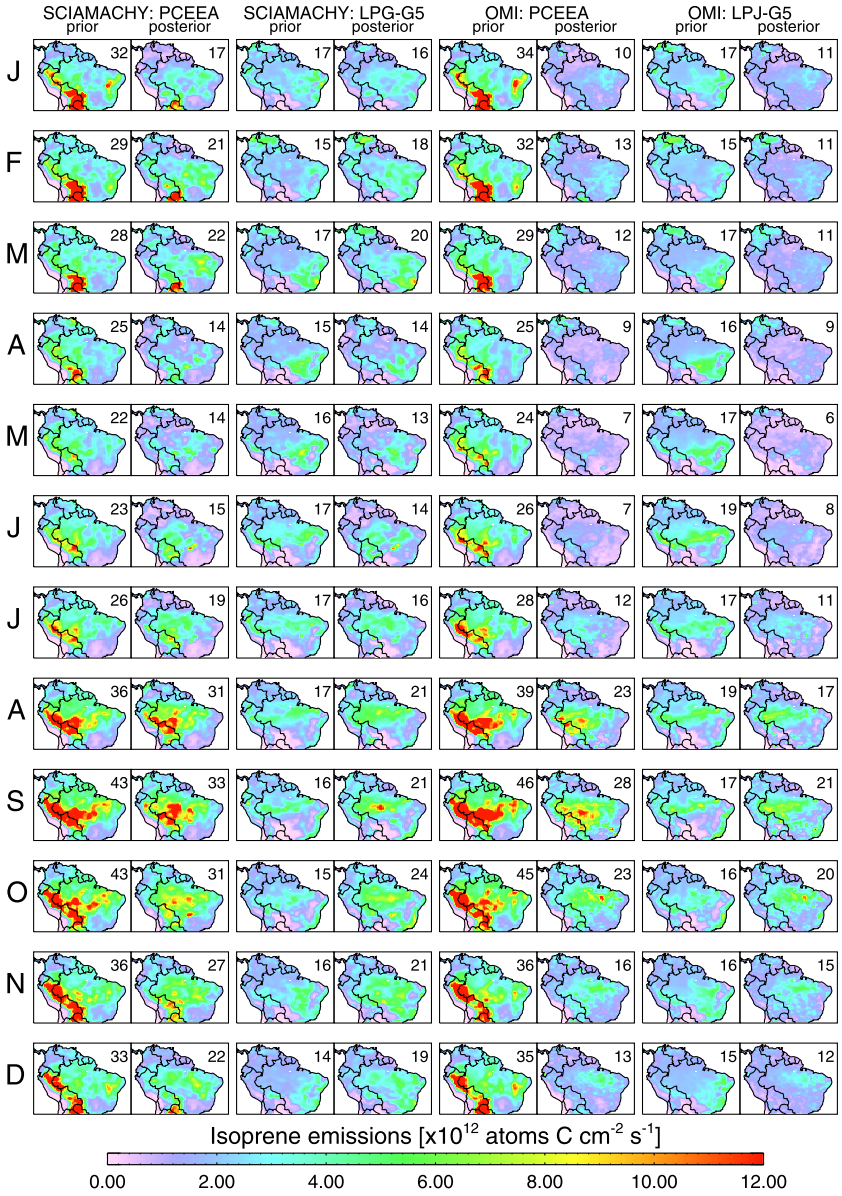

Figure 6. Contiguous maps of prior and posterior isoprene emissions corresponding to the overpasses of SCIAMACHY (9–11 LT) and OMI (12–15 LT) using the PCEEA and LPJ-G5 scenarios (see Table 1 and section 7). The emissions have been smoothed with a 3×3 box-filter (for illustration only); the monthly totals in Tg C are shown inset.

therefore, actually represents a minimum possible value. OMI was sampled on the same days only taking measurements with the aircraft's observing region (i.e., using the maximum and minimum longitude and latitude from all the selected days), and a mean column calculated from all observations, each weighted by its uncertainty. The AMFs for the OMI observations were taken from the PCEEA scenario using corresponding data from October 2006. Compared to the HCHO column constructed from the aircraft measurements, we find the OMI data is about 37% too low over this region and time period. As both retrievals are consistently normalized over the Pacific Ocean, and since spectral fitting drives observed HCHO vertical column variability over the Amazon [*Barkley et al.*, 2012], the origin of this bias must be intrinsic to instrument itself or arise from within the retrieval (e.g., choice of fitting window or technique, HCHO cross section). Increasing the OMI 2006 HCHO vertical columns by 37% yields an ensemble mean of 95 $\pm$ 6 Tg C, which is in much better agreement with SCIAMACHY. The potential OMI bias, also noticed by *De Smedt et al.* [2012], may partly explain some of the disparity between the inferred top-down emissions from the two sensors, but without detailed validation of the satellite data over the Amazon region, it is difficult to draw any firm conclusions.

[47] The alternative option to explain differences between SCIAMACHY and OMI is that the diurnal cycle of isoprene

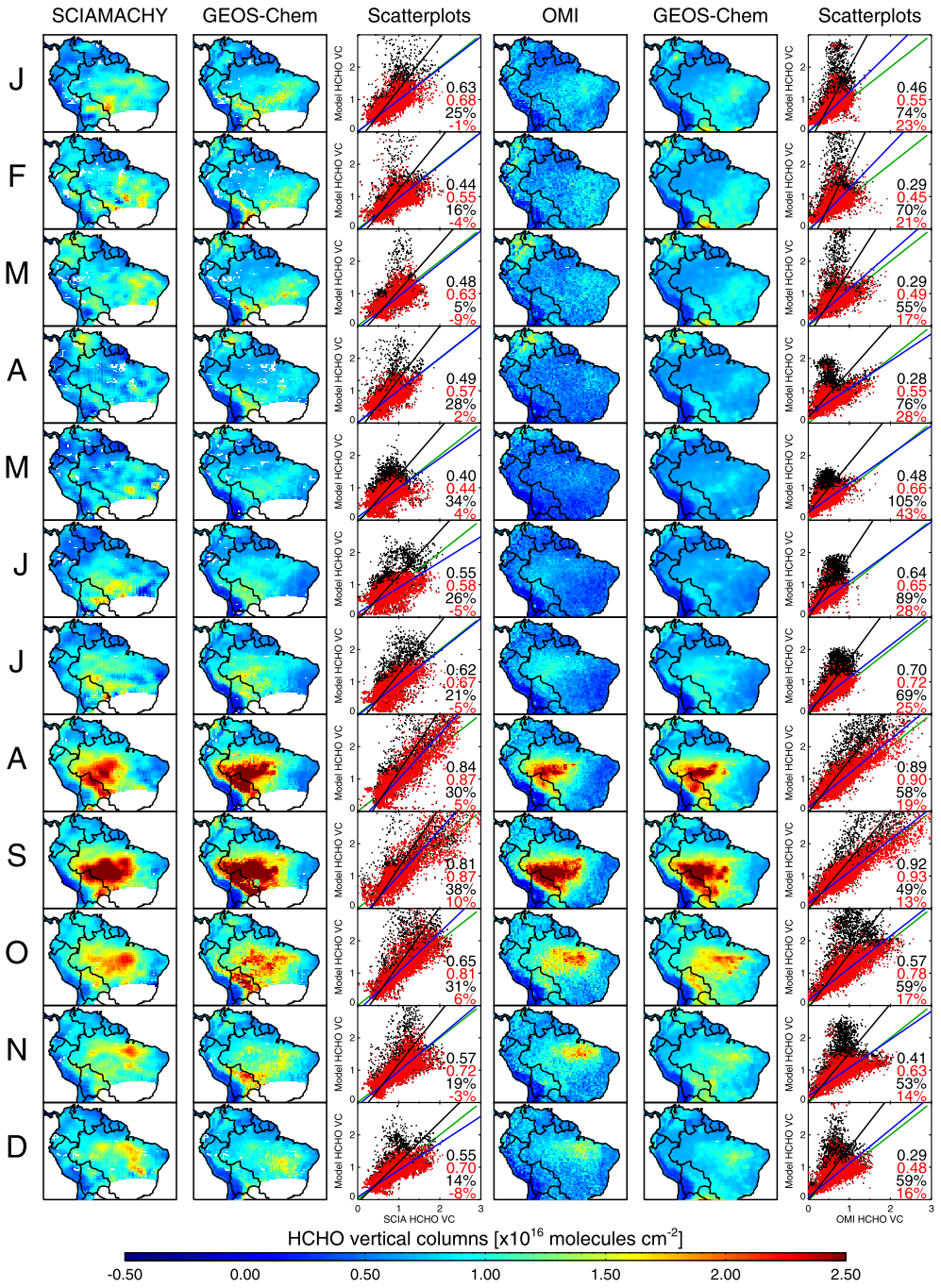

Figure 7. Monthly maps of observed and model HCHO vertical columns showing the effect of driving GEOS-Chem with top-down emissions derived from the PCEEA scenario (cf. Table 1). The first two columns show SCIAMACHY and GEOS-Chem HCHO vertical columns, when the model has been constrained by both SCIAMACHY (at 9–11 LT) and OMI (at 12–15 LT) top-down emissions. The fourth and fifth columns show OMI and GEOS-Chem HCHO vertical columns, when the model has been constrained at all time-steps by OMI top-down emissions alone (see section 7 for details). The corresponding scatterplots show SCIAMACHY and OMI versus GEOS-Chem HCHO vertical columns, that have been simulated using (1) the original prior PCEEA emissions (black dots; black line is reduced major axis fit [*Hirsch and Gilroy*, 1984]) and (2) the inferred top-down emissions (red dots; blue line is regression fit). The $x = y$ line is in green. The normalized mean bias and Pearson correlation coefficients are given inset.

emissions and oxidation chemistry is incorrectly simulated by GEOS-Chem (i.e., the linear transfer functions are not representative of local time conditions). In *Barkley et al.* [2011], we compared the model with in situ TROFFEE campaign data [*Karl et al.*, 2007]. From that comparison it was found that the MEGAN simulated observed emissions reasonably (r = 0.8), but GEOS-Chem struggled to capture the isoprene and MVK+MACR mixing ratios very poorly ($|r| < 0.2$), most likely owing to the poor vertical resolution of the nighttime boundary layer which resulted in significant nocturnal accumulation of isoprene oxidation products in the residual layer. Nevertheless, modeled HCHO columns during the TROFFEE campaign were within about 25% of the mean observed SCIAMACHY vertical column. Additionally, it was found that GEOS-Chem HCHO columns peaked in the night and were a minimum around midday, as also noticed over the southeast US [*Millet et al.*, 2008]. This is in contrast to (daylight) MAX-DOAS measurements over albeit nontropical regions that indicate a peak in the HCHO columns around midday and early afternoon [e.g., *Heckel et al.*, 2005; *De Smedt*, 2011; *Peters et al.*, 2012; *Li et al.*, 2013]. However, without in situ measurements made within the rainforest, it is impossible to establish if GEOS-Chem's diurnal simulation of HCHO over the Amazon is erroneous.

9. Conclusions

[48] We have presented an ensemble of top-down isoprene emissions from tropical South America, inferred from SCIAMACHY and OMI HCHO column observations using a variety of GEOS-Chem and AMF model configurations. Through screening for fires daily using multiple satellite observations of active fire counts and by filtering locations using the model local sensitivity ΔS, we have determined a set of top-down emissions where the influence of biomass burning and spatial smearing is as minor as possible. However, the resulting spatial coverage of the top-down isoprene emissions over the Amazon is particularly poor. Nonetheless, we find in general that the bottom-up emissions need to be reduced significantly to be consistent with HCHO column data, only for LPJ-GUESS-based scenarios do the bottom-up emissions need to be increased. The mean relative differences in the monthly mean emissions over the ensemble are –24 ± 16% for SCIAMACHY, and –48 ± 10% for OMI. Within our modeling system, we find that the retrieved HCHO columns decrease the emission range, or uncertainty, from 27–61 Tg C to 31–38 Tg C for SCIAMACHY, and 45–104 Tg C to 28–38 Tg C for OMI. The calculated mean uncertainties of the top-down emissions are about 60–260% for SCIAMACHY and 10–90% for OMI, though given the large uncertainties associated with simulating tropical isoprene oxidation chemistry, we accept that these errors maybe underestimated. Through relaxation of the ΔS filtering and by filling undetermined locations by scaling the prior emissions, we are able to construct a complete top-down isoprene emission maps for the Amazon region. We find that these steps change the relative differences in the monthly emission totals very little and mainly improve GEOS-Chem's simulation of HCHO columns over the tropical South America, with respect to the SCIAMACHY and OMI data.

[49] Examination of the ensemble top-down emissions and a range of sensitivity tests indicate that the inferred emissions are most affected by uncertainties in cloud fraction and cloud top pressure and the initial bottom-up emission inventory used, though these only cause differences in the annual totals relative to our default scenario of about 10–20%. The results are mostly insensitive to boundary-layer mixing, fast/slow dry deposition, inclusion of hydroxyperoxy aldehydes in the chemical scheme, chemical time step, or AMF surface reflectance. The top-down emissions are also highly sensitive to the treatment of the HCHO data itself, through the reference sector correction and calculation of model specific AMFs. When the local time emissions are scaled to monthly mean emissions, we find that the annual emission totals from SCIAMACHY are nearly twice those determined from OMI. This difference cannot be explained by different sampling characteristics of the sensors or uncertainties associated with the AMF calculation. Therefore, without either validation of the inferred top-down emissions themselves, and/or careful assessment of the satellite HCHO retrievals, we are left rather wondering about the accuracy of the results presented. Development of an adjoint for the GEOS-Chem Amazon nested-grid to perform a formal inversion, will help overcome problematic issues such as spatial smearing and removal of biomass burning contamination, but clearly validation of the HCHO column retrievals over the Amazon remains a priority in order for any top-down isoprene emission estimates to be believed.

[50] **Acknowledgments.** This work was supported by the Natural Environment Research Council (grant NE/GE013810/2). A.A. and D.H. acknowledge support from the Swedish Research Council Formas.

References

Acarreta, J. R., J. F. De Haan, and P. Stammes (2004), Cloud pressure retrieval using the O_{2-2} absorption band at 477 nm, *J. Geophys. Res.*, *109*, D05204, doi:10.1029/2003JD003915.

Archibald, A. T., M. E. Jenkin, and D. E. Shallcross (2010), An isoprene mechanism intercomparison, *Atmos. Environ.*, *44*(40), 5356–5364, doi:10.1016/j.atmosenv.2009.09.016.

Arino, O., S. Plummer, and D. Defrenne (2005), Fire disturbance: The ten years time series of the ATSR World Fire Atlas, in *MERIS-AATSR Workshop 2005, Frascati, Italy, September, 2005*, edited by H. Lacoste, Eur. Space Agency, Frascati, Italy.

Arneth, A., et al. (2007), Process-based estimates of terrestrial ecosystem isoprene emissions: Incorporating the effects of a direct CO_2-isoprene interaction, *Atmos. Chem. Phys.*, *7*(1), 31–53, doi:10.5194/acp-7-31-2007.

Arneth, A., R. K. Monson, G. Schurgers, U. Niinemets, and P. I. Palmer (2008), Why are estimates of global terrestrial isoprene emissions so similar (and why is this not so for monoterpenes)? *Atmos. Chem. Phys.*, *8*(16), 4605–4620, doi:10.5194/acp-8-4605-2008.

Arneth, A., G. Schurgers, J. Lathiere, T. Duhl, D. J. Beerling, C. N. Hewitt, M. Martin, and A. Guenther (2011), Global terrestrial isoprene emission models: Sensitivity to variability in climate and vegetation, *Atmos. Chem. Phys.*, *11*(15), 8037–8052, doi:10.5194/acp-11-8037-2011.

Ashworth, K., O. Wild, and C. N. Hewitt (2010), Sensitivity of isoprene emissions estimated using MEGAN to the time resolution of input climate data, *Atmos. Chem. Phys.*, *10*(3), 1193–1201, doi:10.5194/acp-10-1193-2010.

Barkley, M. P., P. I. Palmer, U. Kuhn, J. Kesselmeier, K. Chance, T. P. Kurosu, R. V. Martin, D. Helmig, and A. Guenther (2008), Net ecosystem fluxes of isoprene over tropical South America inferred from GOME observations of HCHO columns, *J. Geophys. Res.*, *113*, D20304, doi:10.1029/2008JD009863.

Barkley, M. P., P. I. Palmer, I. D. Smedt, T. Karl, A. Guenther, and M. V. Roozendael (2009), Regulated large-scale annual shutdown of Amazonian isoprene emissions? *Geophys. Res. Lett.*, *36*, L04803, doi:10.1029/2008GL036843.

Barkley, M. P., et al. (2011), Can a 'state of the art' chemistry transport model simulate Amazonian tropospheric chemistry? *J. Geophys. Res.*, *116*, D16302, doi:10.1029/2011JD015893.

Barkley, M. P., T. P. Kurosu, K. Chance, I. D. Smedt, M. V. Roozendael, A. Arneth, D. Hagberg, and A. Guenther (2012), Assessing sources of uncertainty in formaldehyde air-mass factors over tropical South America: Implications for top-down isoprene emission estimates, *J. Geophys. Res.*, *117*, D13304, doi:10.1029/2011JD016827.

Bovensmann, H., J. P. Burrows, M. Buchwitz, J. Frerick, S. Nöel, V. V. Rozanov, K. V. Chance, and A. Goede (1999), SCIAMACHY–Mission objectives and measurement modes, *J. Atmos. Sci.*, *56*, 127–150.

Cantrell, C. A., J. A. Davidson, A. H. McDaniel, R. E. Shetter, and J. G. Calvert (1990), Temperature-dependent formaldehyde cross sections in the near-ultraviolet spectral region, *J. Phys. Chem.*, *94*, 3902–3908.

Chance, K. (2002), OMI algorithm theoretical basis document, volume IV, OMI trace gas algorithms, OMI-ATBD-VOL4, ATBD-OMI-04, Version 2.0, NASA, GES-DISC, Goddard Earth Sciences Data and Information Service Center.

Chance, K., and R. Spurr (1997), Ring effect studies: Rayleigh scattering, including molecular parameters for rotational Raman scattering, and the Fraunhofer spectrum, *Appl. Opt.*, *36*(21), 5224–5230, doi:10.1364/AO.36.005224.

Crounse, J. D., F. Paulot, H. G. Kjaergaard, and P. O. Wennberg (2011), Peroxy radical isomerization in the oxidation of isoprene, *Phys. Chem. Chem. Phys.*, *13*, 13607–13613, doi:10.1039/c1cp21330j.

De Smedt, I. (2011), Long-term global observations of tropospheric formaldehyde retrieved from spaceborne nadir UV sensors, PhD thesis, Fac. of Appl. Sci., University of Brussels, Brussels.

De Smedt, I., J.-F. Müller, T. Stavrakou, R. van der, A. H. Eskes, and M. V. Roozendael (2008), Twelve years of global observation of formaldehyde in the troposphere using GOME and SCIAMACHY sensors, *Atmos. Chem. Phys.*, *8*, 4947–4963, doi:10.5194/acp-8-4947-2008.

De Smedt, I., M. Van Roozendael, T. Stavrakou, J.-F. Müller, K. Chance, and T. Kurosu (2012), Intercomparison of 4 years of global formaldehyde observations from the GOME-2 and OMI sensors, in *ESA-ATMOS 2012 Atmospheric Science Conference*, edited by L. Ouwehand, Eur. Space Agency, Bruges, Belgium.

Fortems-Cheiney, A., et al. (2012), The formaldehyde budget as seen by a global-scale multi-constraint and multi-species inversion system, *Atmos. Chem. Phys.*, *12*(15), 6699–6721, doi:10.5194/acp-12-6699-2012.

Fu, T.-M., D. J. Jacob, P. I. Palmer, K. Chance, Y. X. Wang, B. Barletta, D. R. Blake, J. C. Stanton, and M. J. Pilling (2007), Space-based formaldehyde measurements as constraints on volatile organic compound emissions in east and south Asia and implications for ozone, *J. Geophys. Res.*, *112*, D06312, doi:10.1029/2006JD007853.

Giglio, L., J. Descloitres, C. O. Justice, and Y. J. Kaufman (2003), An enhanced contextual fire detection algorithm for MODIS, *Remote Sens. Environ.*, *87*(2–3), 273–282, doi:10.1016/S0034-4257(03)00184-6.

Giglio, L., I. Csiszar, and C. Justice (2006), Global distribution and seasonality of active fires as observed with the Terra and Aqua MODIS sensors, *Biogeosciences*, *111*, G02016, doi:10.1029/2005JG000142.

Gonzi, S., P. I. Palmer, M. P. Barkley, I. D. Smedt, and M. V. Roozendael (2011), Biomass burning emission estimates inferred from satellite column measurements of HCHO: Sensitivity to co-emitted aerosol and injection height, *Geophys. Res. Lett.*, *38*, L14807, doi:10.1029/2011GL047890.

Guenther, A., et al. (1995), A global model of natural volatile organic compound emissions, *J. Geophys. Res.*, *100*(D5), 8873–8892, doi:10.1029/94JD02950.

Guenther, A., B. Baugh, G. Brasseur, J. Greenberg, P. Harley, L. Klinger, D. Serça, and L. Vierling (1999), Isoprene emission estimates and uncertainties for the Central African EXPRESSO study domain, *J. Geophys. Res.*, *104*(D23), 30,625–30,639.

Guenther, A., T. Karl, P. Harley, C. Wiedinmyer, P. I. Palmer, and C. Geron (2006), Estimates of global terrestrial isoprene emissions using MEGAN (model of emissions of gases and aerosols from nature), *Atmos. Chem. Phys.*, *6*, 3181–3210, doi:10.5194/acp-6-3181-2006.

Heckel, A., A. Richter, T. Tarsu, F. Wittrock, C. Hak, I. Pundt, W. Junkermann, and J. P. Burrows (2005), MAX-DOAS measurements of formaldehyde in the Po-Valley, *Atmos. Chem. Phys.*, *5*(4), 909–918, doi:10.5194/acp-5-909-2005.

Herman, J. R., and E. A. Celarier (1997), Earth surface reflectivity climatology at 340–380 nm from TOMS data, *J. Geophys. Res.*, *102*(D23), 28,003–28,011, doi:doi:10.1029/97JD02074.

Hirsch, R. M., and E. J. Gilroy (1984), Methods of fitting a straight line to data: Examples in water resourses, *Water Res. Bull.*, *20*, 705–711.

Jacobson, M. Z. (1995), Computation of global photochemistry with SMVGEAR-II, *Atmos. Environ.*, *29*, 2541–2546.

Kanakidou, M., et al. (2005), Organic aerosol and global climate modelling: A review, *Atmos. Chem. Phys.*, *5*(4), 1053–1123, doi:10.5194/acp-5-1053-2005.

Karl, T., A. Guenther, R. J. Yokelson, J. Greenberg, M. Potosnak, D. R. Blake, and P. Artaxo (2007), The tropical forest and fire emissions experiment: Emission, chemistry, and transport of biogenic volatile organic compounds in the lower atmosphere over Amazonia, *J. Geophys. Res.*, *112*, D18302, doi:10.1029/2007JD008539.

Karl, T., P. Harley, L. Emmons, B. Thornton, A. Guenther, C. Basu, A. Turnipseed, and K. Jardine (2010), Efficient atmospheric cleansing of oxidized organic trace gases by vegetation, *Science*, *330*, 816–819, doi:10.1126/science.1192534.

Kesselmeier, J., and M. Staudt (1999), Biogenic Volatile Organic Compounds (VOC): An overview on emission, physiology and ecology, *J. Atmos. Chem.*, *33*, 23–88.

Kleipool, Q. L., M. R. Dobber, J. F. de Haan, and P. F. Levelt (2008), Earth surface reflectance climatology from 3 years of OMI data, *J. Geophys. Res.*, *113*, D18308, doi:10.1029/2008JD010290.

Kuhn, U., et al. (2004), Seasonal differences in isoprene and light-dependent monoterpene emission by Amazonian tree species, *Global Change Biol.*, *10*, 663–682, doi:10.1111/j.1529-8817.2003.00771.x.

Kuhn, U., et al. (2007), Isoprene and monoterpene fluxes from Central Amazonian rainforest inferred from tower-based and airborne measurements, and implications on the atmospheric chemistry and the local carbon budget, *Atmos. Chem. Phys.*, *7*, 2855–2879, doi:10.5194/acp-7-2855-2007.

Kurosu, T. P., and K. Chance (2008), *OMHCHO readme file, Harvard-Smithson. Cent. for Astrophys.*, Cambridge, MA, USA.

Laothawornkitkul, J., J. E. Taylor, N. D. Paul, and C. N. Hewitt (2009), Biogenic volatile organic compounds in the Earth system, *New Phytol.*, *183*, 27–51.

Lathière, J., C. N. Hewitt, and D. J. Beerling (2010), Sensitivity of isoprene emissions from the terrestrial biosphere to 20th century changes in atmospheric CO_2 concentration, climate, and land use, *Global Biogeochem. Cycles*, *24*, GB1004, doi:10.1029/2009GB003548.

Lelieveld, J., et al. (2008), Atmospheric oxidation capacity sustained by a tropical forest, *Nature*, *452*, 737–740, doi:10.1038/nature06870.

Levelt, P. F., et al. (2006), The Ozone monitoring instrument, *IEEE Trans. Geosci. Remote Sens.*, *44*(5), 1093–1101, doi:10.1109/TGRS.2006.872333.

Li, X., T. Brauers, A. Hofzumahaus, K. Lu, Y. P. Li, M. Shao, T. Wagner, and A. Wahner (2013), MAX-DOAS measurements of NO_2, HCHO and CHOCHO at a rural site in Southern China, *Atmos. Chem. Phys.*, *13*(4), 2133–2151, doi:10.5194/acp-13-2133-2013.

Lin, J.-T., and M. B. McElroy (2010), Impacts of boundary layer mixing on pollutant vertical profiles in the lower troposphere: Implications to satellite remote sensing, *Atmos. Environ.*, *44*, 1726–1739.

Liu, H. Y., D. J. Jacob, I. Bey, and R. M. Yantosca (2001), Constraints from Pb-210 and Be-7 on wet deposition and transport in a global three-dimensional chemical tracer model driven by assimilated meteorological fields, *J. Geophys. Res.*, *106*, 12,109–12,128.

Lockwood, A. L., P. B. Shepson, M. N. Fiddler, and M. Alaghmand (2010), Isoprene nitrates: Preparation, separation, identification, yields, and atmospheric chemistry, *Atmos. Chem. Phys.*, *10*(13), 6169–6178, doi:10.5194/acp-10-6169-2010.

Mao, J., et al. (2012), Insights into hydroxyl measurements and atmospheric oxidation in a California forest, *Atmos. Chem. Phys.*, *12*(17), 8009–8020, doi:10.5194/acp-12-8009-2012.

Marais, E. A., et al. (2012), Isoprene emissions in Africa inferred from OMI observations of formaldehyde columns, *Atmos. Chem. Phys.*, *12*(14), 6219–6235, doi:10.5194/acp-12-6219-2012.

Mari, C., D. J. Jacob, and P. Bechtold (2000), Transport and scavenging of soluble gases in a deep convective cloud, *J. Geophys. Res.*, *105*, 22,255–22,267.

Martin, R. V., et al. (2002), An improved retrieval of tropospheric nitrogen dioxide from GOME, *J. Geophys. Res.*, *107*(D20), 4437, doi:10.1029/2001JD001027.

Martin, R. V., D. J. Jacob, R. M. Yantosca, M. Chin, and P. Ginoux (2003), Global and regional decreases in tropospheric oxidants from photochemical effects of aerosols, *J. Geophys. Res.*, *108*(D3), 4097, doi:10.1029/2002JD002622.

Meller, R., and G. K. Moortgat (2000), Temperature dependence of the absorption cross sections of formaldehyde between 223 and 323 K in the wavelength range 225–375 nm, *J. Geophys. Res.*, *105*(D6), 7089–7101, doi:10.1029/1999JD901074.

Millet, D. B., D. J. Jacob, K. Folkert Boersma, T.-M. Fu, T. P. Kurosu, K. Chance, C. L. Heald, and A. Guenther (2008), Spatial distribution of isoprene emissions from North America derived from formaldehyde column measurements by the OMI satellite sensor, *J. Geophys. Res.*, *113*, D02307, doi:10.1029/2007JD008950.

Mollner, A. K., et al. (2010), Rate of Gas Phase Association of Hydroxyl Radical and Nitrogen Dioxide, *Science*, *330*(6004), 646–649, doi:10.1126/science.1193030.

Müller, J.-F., et al. (2008), Global isoprene emissions estimated using MEGAN, ECMWF analyses and a detailed canopy environment model, *Atmos. Chem. Phys.*, *8*(5), 1329–1341, doi:10.5194/acp-8-1329-2008.

Nichitiu, F., J. R. Drummond, J. Zou, and R. Deschambault (2004), Solar particle events seen by the MOPITT instrument, *J. Atmos. Sol. Terr. Phys.*, *66*, 1797–1803, doi:10.1016/j.jastp.2004.06.002.

Niinemets, U., J. D. Tenhunen, P. C. Harley, and R. Steinbrecher (1999), A model of isoprene emission based on energetic requirements for isoprene synthesis and leaf photosynthetic properties for Liquidambar and Quercus, *Plant Cell Environ.*, *22*(17), 1319–1335, doi:10.1046/j.1365-3040.1999.00505.x.

Palmer, P. I. et al. (2001), Air mass factor formulation for spectroscopic measurements from satellites: Application to formaldehyde retrievals from the Global Ozone Monitoring Experiment, *J. Geophys. Res.*, *106*, 14,539–14,550, doi:10.1029/2000JD900772.

Palmer, P. I., D. J. Jacob, A. M. Fiore, R. V. Martin, K. Chance, and T. P. Kurosu (2003), Mapping isoprene emissions over North America using formaldehyde column observations from space, *J. Geophys. Res.*, *108*(D6), 4180, doi:10.1029/2002JD002153.

Palmer, P. I., et al. (2006), Quantifying the seasonal and interannual variability of North American isoprene emissions using satellite observations of formaldehyde column, *J. Geophys. Res.*, *111*, D12315, doi:10.1029/2005JD006689.

Paulot, F., J. D. Crounse, H. G. Kjaergaard, J. H. Kroll, J. H. Seinfeld, and P. O. Wennberg (2009a), Isoprene photooxidation: New insights into the production of acids and organic nitrates, *Atmos. Chem. Phys.*, *9*(4), 1479–1501, doi:10.5194/acp-9-1479-2009.

Paulot, F., J. D. Crounse, H. G. Kjaergaard, A. Kurten, J. M. St. Clair, J. H. Seinfeld, and P. O. Wennberg (2009b), Unexpected epoxide formation in the gas-phase photooxidation of isoprene, *Science*, *325*(5941), 730–733, doi:10.1126/science.1172910.

Paulot, F., D. K. Henze, and P. O. Wennberg (2012), Impact of the isoprene photochemical cascade on tropical ozone, *Atmos. Chem. Phys.*, *12*(3), 1307–1325, doi:10.5194/acp-12-1307-2012.

Peeters, J., and J.-F. Müller (2010), HO_x radical regeneration in the isoprene oxidation via peroxy radical isomerisations. II: Experimental evidence and global impact, *Phys. Chem. Chem. Phys.*, *12*, 14,227–14,235, doi:10.1039/c0cp00811g.

Peeters, J., T. L. Nguyen, and L. Vereecken (2009), HO_x radical regeneration in the oxidation of isoprene, *Phys. Chem. Chem. Phys.*, *11*, 5935–5939, doi:10.1039/b908511d.

Peters, E., F. Wittrock, K. Großmann, U. Frieß, A. Richter, and J. P. Burrows (2012), Formaldehyde and nitrogen dioxide over the remote western Pacific Ocean: SCIAMACHY and GOME-2 validation using ship-based MAX-DOAS observations, *Atmos. Chem. Phys.*, *12*(22), 11,179–11,197, doi:10.5194/acp-12-11179-2012.

Rienecker, M., et al. (2008), The GEOS-5 Data Assimilation System—Documentation of versions 5.0.1, 5.1.0, and 5.2.0, in *Technical Report Series on Global Modeling and Data Assimilation,* vol. 27, NASA Tech. Memo., NASA/TM-2008-104606.

Sander, S. P., et al., (2011), Chemical kinetics and photochemical data for use in atmospheric studies, evaluation number 17, *JPL Publ. 10-6.*, Jet Propul. Lab., Pasadena, Calif.

Saunders, S. M., M. E. Jenkin, R. G. Derwent, and M. J. Pilling (2003), Protocol for the development of the Master Chemical Mechanism, MCM v3 (Part A): Tropospheric degradation of non-aromatic volatile organic compounds, *Atmos. Chem. Phys.*, *3*(1), 161–180, doi:10.5194/acp-3-161-2003.

Spurr, R. J. D., T. P. Kurosu, and K. Chance (2001), A linearized discrete ordinate radiative transfer model for atmospheric remote sensing retrieval, *J. Quant. Spectrosc. Radiat. Transfer*, *68*(6), 689–735.

Stavrakou, T., J.-F. Müller, I. De Smedt, M. Van Roozendael, G. R. van der Werf, L. Giglio, and A. Guenther (2009a), Global emissions of non-methane hydrocarbons deduced from SCIAMACHY formaldehyde columns through 2003–2006, *Atmos. Chem. Phys.*, *9*(11), 3663–3679, doi:10.5194/acp-9-3663-2009.

Stavrakou, T., J.-F. Müller, I. De Smedt, M. Van Roozendael, G. R. van der Werf, L. Giglio, and A. Guenther (2009b), Evaluating the performance of pyrogenic and biogenic emission inventories against one decade of space-based formaldehyde columns, *Atmos. Chem. Phys.*, *9*(3), 1037–1060, doi:10.5194/acp-9-1037-2009.

Stavrakou, T., J. Peeters, and J.-F. Müller (2010), Improved global modelling of HO_x recycling in isoprene oxidation: Evaluation against the GABRIEL and INTEX-A aircraft campaign measurements, *Atmos. Chem. Phys.*, *10*(20), 9863–9878, doi:10.5194/acp-10-9863-2010.

Stickler, A., et al. (2007), Chemistry, transport and dry deposition of trace gases in the boundary layer over the tropical Atlantic Ocean and the Guyanas during the GABRIEL field campaign, *Atmos. Chem. Phys.*, *7*(14), 3933–3956, doi:10.5194/acp-7-3933-2007.

Taraborrelli, D., M. G. Lawrence, T. M. Butler, R. Sander, and J. Lelieveld (2009), Mainz Isoprene Mechanism 2 (MIM2): An isoprene oxidation mechanism for regional and global atmospheric modelling, *Atmos. Chem. Phys.*, *9*(8), 2751–2777, doi:10.5194/acp-9-2751-2009.

Taraborrelli, D., M. G. Lawrence, J. N. Crowley, S. Gromov, C. B. M. Grosz, L. Vereecken, and J. Lelieveld (2012), Hydroxyl radical buffered by isoprene oxidation over tropical forests, *Nat. Geosci.*, *5*, 190–193, doi:10.1038/ngeo1405.

Turner, A. J., D. K. Henze, R. V. Martin, and A. Hakami (2012), The spatial extent of source influences on modeled column concentrations of short-lived species, *Geophys. Res. Lett.*, *39*, L12806, doi:10.1029/2012GL051832.

van der Werf, G. R., J. T. Randerson, L. Giglio, G. J. Collatz, P. S. Kasibhatla, and A. F. Arellano Jr (2006), Interannual variability in global biomass burning emissions from 1997 to 2004, *Atmos. Chem. Phys.*, *6*(11), 3423–3441, doi:10.5194/acp-6-3423-2006.

Wang, P., P. Stammes, R. van der A, G. Pinardi, and M. van Roozendael (2008), FRESCO+: An improved O_2 A-band cloud retrieval algorithm for tropospheric trace gas retrievals, *Atmos. Chem. Phys.*, *8*(21), 6565–6576, doi:10.5194/acp-8-6565-2008.

Wang, Y., D. J. Jacob, and J. A. Logan (1998), Global simulation of tropospheric O_3-NO_x-hydrocarbon chemistry 1. Model formulation, *J. Geophys. Res.*, *103*, 10,713–10,726, doi:10.1029/98JD00158.

Wesely, M. L. (1989), Parameterization of surface resistances to gaseous dry deposition in regional scale numerical models, *Atmos. Environ.*, *23*, 1293–1304.

Wild, O., X. Zhu, and M. J. Prather (2000), Fast-J: Accurate simulation of in- and below-cloud photolysis in tropospheric chemical models, *J. Atmos. Chem.*, *37*, 245–282.